Image super-resolution: The techniques, applications, and future

6 authors, including:

Linwei Yue
China University of Geosciences
23 PUBLICATIONS   392 CITATIONS

SEE PROFILE

Jie Li
Wuhan University
35 PUBLICATIONS   518 CITATIONS

SEE PROFILE

Qiangqiang Yuan
Wuhan University
118 PUBLICATIONS   2,876 CITATIONS

SEE PROFILE

Hongyan Zhang
Wuhan University
85 PUBLICATIONS   3,135 CITATIONS

SEE PROFILE

Some of the authors of this publication are also working on these related projects:

Information Mining from Remote Sensing Big Data View project

Deep learning in remote sensing View project

Review

Image super-resolution: The techniques, applications, and future

CrossMark

Linwei Yue [a], Huanfeng Shen [b,c,*], Jie Li [a], Qiangqiang Yuan [c,d], Hongyan Zhang [a,c], Liangpei Zhang [a,c,*]

[a] The State Key Laboratory of Information Engineering in Surveying, Mapping and Remote Sensing, Wuhan University, Wuhan, PR China
[b] School of Resource and Environmental Science, Wuhan University, Wuhan, PR China
[c] Collaborative Innovation Center of Geospatial Technology, Wuhan University, Wuhan, PR China
[d] School of Geodesy and Geomatics, Wuhan University, Wuhan, PR China

ABSTRACT

Super-resolution (SR) technique reconstructs a higher-resolution image or sequence from the observed LR images. As SR has been developed for more than three decades, both multi-frame and single-frame SR have significant applications in our daily life. This paper aims to provide a review of SR from the perspective of techniques and applications, and especially the main contributions in recent years. Regularized SR methods are most commonly employed in the last decade. Technical details are discussed in this article, including reconstruction models, parameter selection methods, optimization algorithms and acceleration strategies. Moreover, an exhaustive summary of the current applications using SR techniques has been presented. Lastly, the article discusses the current obstacles for future research.

© 2016 Elsevier B.V. All rights reserved.

Contents

* Corresponding authors at: School of Resource and Environmental Science, Wuhan University, Wuhan, PR China.
  E-mail addresses: shenhf@whu.edu.cn (H. Shen), zlp62@whu.edu.cn (L. Zhang).

1. Introduction

Image spatial resolution refers to the capability of the sensor to observe or measure the smallest object, which depends upon the pixel size. As two-dimensional signal records, digital images with a higher resolution are always desirable in most applications. Imaging techniques have been rapidly developed in the last decades, and the resolution has reached a new level. The question is therefore: are image resolution enhancement techniques still required?

The fact is, although the high-definition displays in recent years have reached a new level (e.g., 1920*1080 for HDTV, 3840*2160 for some ultra HDTV, and 2048*1536 for some mobile devices), the need for resolution enhancement cannot be ignored in many applications [1]. For instance, to guarantee the long-term stable operation of the recording devices, as well as the appropriate frame rate for dynamic scenes, digital surveillance products tend to sacrifice resolution to some degree. A similar situation exists in the remote sensing field: there is always a tradeoff between the spatial, spectral, and temporal resolutions. As for medical imaging, within each imaging modality, specific physical laws are in control, defining the meaning of noise and the sensitivity of the imaging process. How to extract 3D models of the human structure with high-resolution images while reducing the level of radiation still remains a challenge [2,3].

Based on these facts, the current techniques cannot yet satisfy the demands. Resolution enhancement is therefore still necessary, especially in fields such as video surveillance, medical diagnosis, and remote sensing applications. Considering the high cost and the limitations of resolution enhancement through "hardware" techniques, especially for large-scale imaging devices, signal processing methods, which are known as super-resolution (SR), have become a potential way to obtain high-resolution (HR) images. With SR methods, we can go beyond the limit of the low-resolution (LR) observations, rather than improving the hardware devices.

SR is a technique which reconstructs a higher-resolution image or sequence from the observed LR images. Technically, SR can be categorized as multi-frame or single-frame based on the input LR information [4–8]. If multiple images of the same scene with sub-pixel misalignment can be acquired, the complementary information between them can be utilized to reconstruct a higher-resolution image or image sequence, as Fig. 1 shows. However, multiple LR images may sometimes not be available for the reconstruction, and thus we need to recover the HR image using the limited LR information, which is defined as single-frame SR [9–12].

Although SR techniques have been comprehensively summarized in several studies [4,6,8,13–15], this paper aims to provide a review from the perspective of techniques and applications, and especially the main contributions in recent decades. This paper provides a more detailed description of the most commonly employed regularized SR methods, including fidelity models, regularization models, parameter estimation methods, optimization algorithms, acceleration strategies, etc. Moreover, we present an exhaustive summary of the current applications using SR techniques, such as the recent Google Skybox satellite application [16] and unmanned aerial vehicle (UAV) surveillance sequences [17]. The current obstacles for the future research are also discussed.

2. Technical background

Nowadays, charge-coupled devices (CCDs) and complementary metal oxide semiconductors (CMOSs) are the most widely used image sensors [4,18]. To obtain an HR image, one of the solutions is to develop more advanced optical devices. As the spatial resolution is governed by the CCD array and optical lens, reducing the pixel size is one of the most direct approaches to increase the spatial resolution. However, as the pixel size decreases, the amount of available light also decreases, and the image quality becomes severely degraded by shot noise. Furthermore, non-rectangular pixel layouts, as in the hexagonal Fujifilm super CCD and the orthogonal-transfer CCD [18,19], have been used to increase the spatial sampling rate, as shown in Fig. 2. Other approaches include increasing the focal length or the chip size. However, a longer focal length will lead to an increase in the size and weight of cameras, while a larger chip size will result in an increase in capacitance. Therefore, both of these approaches are not considered to be effective due to the limitations of the sensors and the optics manufacturing technology [4]. Compared with CMOSs, CCDs have advantages in sensor sensitivity, imaging resolution, noise suppression and technology maturity [20]. However, considering the high cost of current CCD-based cameras, CMOS-based technologies have recently been investigated. For example, Scientific CMOS (sCMOS) sensors feature a higher resolution and high signal-to-noise ratio (SNR); however, the practical use of this technology remains a problem [21]. Overall, due to the limitations of hardware technology, it is still necessary to study SR algorithms to achieve the goal of resolution enhancement.

Based on the concept of SR, the first problem we need to discuss is the conditions to obtain an HR image from multiple LR observed images. In general, if there is supplementary information among the images, SR is feasible [22]. That is to say, the LR observations cannot be obtained from each other by a transformation or resampling process, thus they contain different information
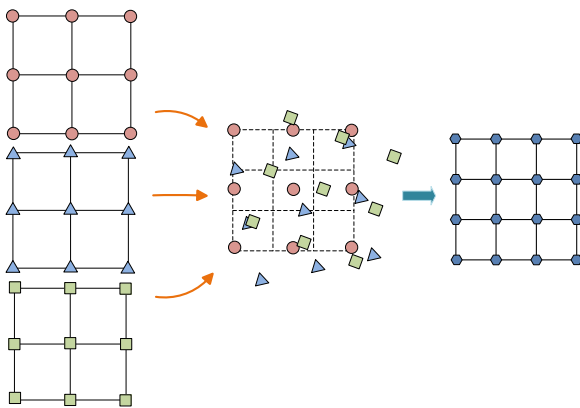
Fig. 1. The concept of multi-frame super-resolution. The grids on the left side represent the LR images of the same scene with sub-pixel alignment, thus the HR image (the grid on the right side) can be acquired by fusing the complementary information with SR methods.
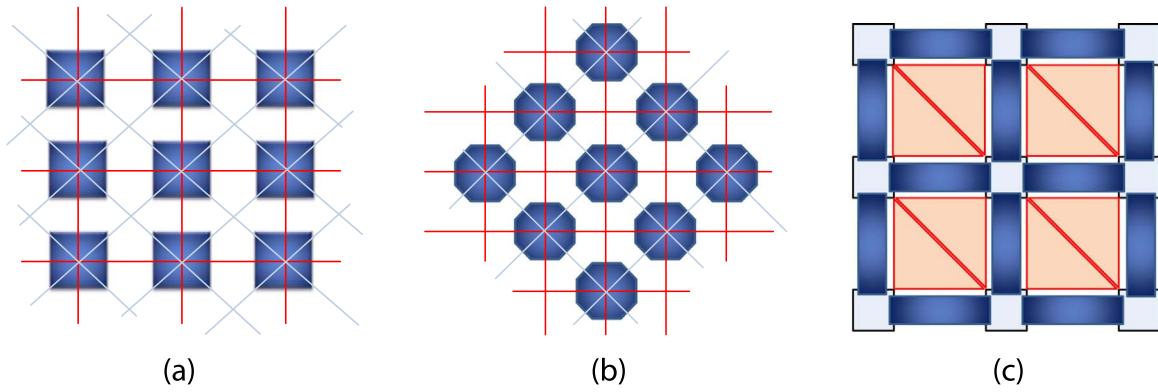
Fig. 2. The basic CCD types [18]: (a) conventional CCD, (b) super CCD with a nonrectangular pixel layout, and (c) orthogonal-transfer CCD.
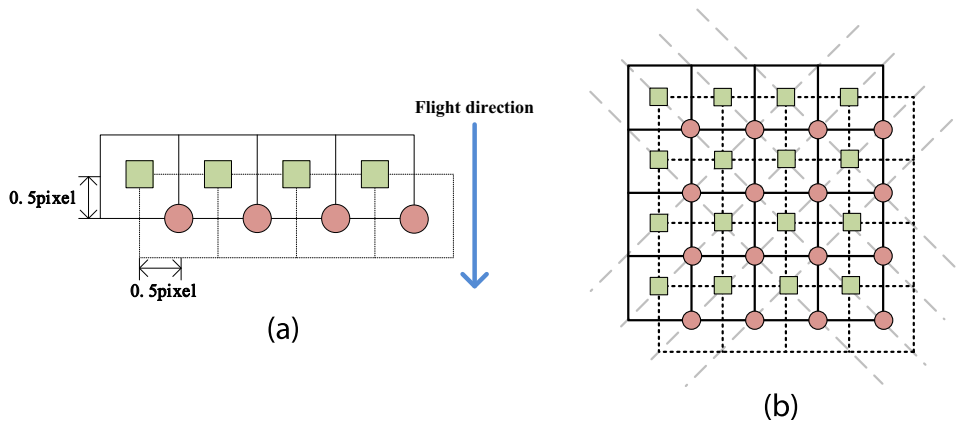

Fig. 3. Sub-pixel imaging for SPOT-5 [23]. A double CCD linear array in (a) generates two classical square sampling grids in (b), shifted by half a sampling interval in both row and column directions.

which can be used for SR. If the relative shifts between the LR images are integral, the images after motion registration will contain almost the same information. As a result, SR cannot obtain effective results.

To implement SR in a real application, researchers have attempted to acquire the images for SR through hardware control. By means of designing the imaging mechanism by hardware techniques, the sensors can acquire observations with known sub-pixel displacements, or multiple "looks" for the same scene. SR is therefore possible. Successful examples can be found in various fields [2,23–26]. One of the most famous successful cases is in the field of remote sensing. In the French space agency's SPOT-5 satellite system, a specially developed CCD detector was used which packages two 12,000-pixel CCDs in one structure. Two line-array CCDs are shifted with each other by half a pixel width in the line-array direction, as shown in Fig. 3 [23]. Since the two CCD detectors can capture images at the same time, a set of data can therefore be acquired at a half-pixel shift in the imaging position. Using this device and SR techniques, we can obtain a HR image from the two sub-pixel shifted images. Leica ADS40 aerial cameras have adopted a similar imaging mechanism to SPOT-5 [27,28]. Moreover, some CCD pixels comprise sub-pixels with different shapes and spatial locations [29]. By combining multiple images recorded with different sub-pixel components, we can obtain a higher-resolution image via SR.

3. Super-resolution technologies and methods

In this part, we discuss the methods and current problems for SR with multiple observations. The key problem is how to use the

supplementary information among the acquired repeat-pass images. In 1964, Harris [30] established the theoretical foundation for the SR problem by introducing the theorems of how to solve the diffraction problem in an optical system. Two decades later, Tsai and Huang [31] first addressed the idea of SR to improve the spatial resolution of Landsat TM images. Since then, many researchers have begun to focus on SR, either in theoretical research or practical applications [1,2,22,24–26,28,32–70]. SR has now been developed for more than three decades, and the progress of SR can be roughly summarized as follows.

At the very start, most of the methods concentrated on the frequency domain [31,33,59–61]. Frequency domain algorithms can make use of the relationship between the HR image and the LR observations based on a simple theoretical basis, and have high computational efficiency. However, the methods have apparent limitations, such as sensitivity to model errors and difficulty in handling more complicated motion models, which have prevented them from further development.

Due to the drawbacks of the frequency domain algorithms, spatial domain methods then became the main trend [4]. The popular spatial domain methods include non-uniform interpolation [35], iterative back-projection (IBP) [56], projection onto convex sets (POCS) [57,63,70], the regularized methods [34,40,43,47,53,54,58,62], and a number of hybrid algorithms [71]. Early review papers have provided specific descriptions and explanations of those methods [4,8,14]. Among them, the regularized methods are the most popular due to their effectiveness and flexibility. Therefore, most of the recent representative articles about SR have focused on regularized frameworks [1,47,49,53,54,68,72,73]. In this part, our emphasis is to review the development of the regularized methods, especially over the last

Ill-posed inverse problem
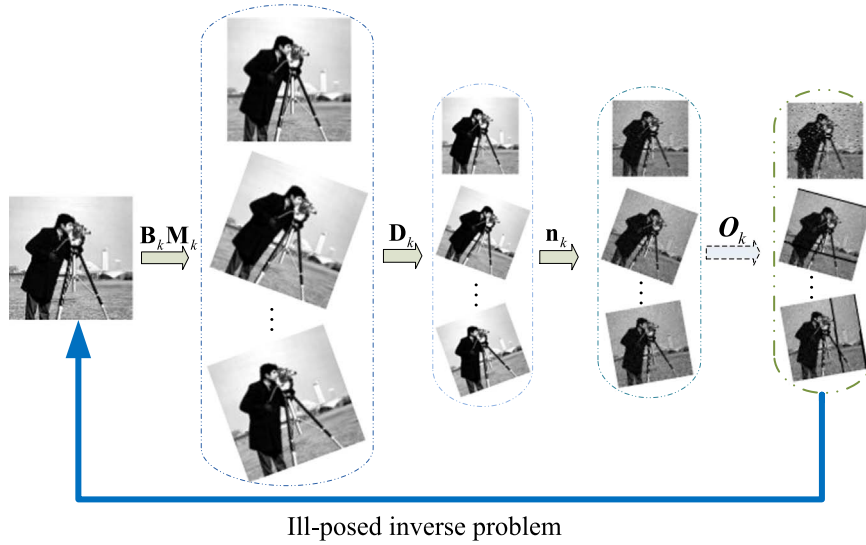
Fig. 4. The super-resolution imaging model. $\boldsymbol{B}_k$, $\boldsymbol{M}_k$ and $\boldsymbol{D}_k$ indicate the blur matrix, warp matrix and down-sampling matrix, respectively. $\boldsymbol{n}_k$ represents the additive noise, while $\boldsymbol{O}_k$ is the operator cropping the observable pixels from $\boldsymbol{y}_k$.

decade. Furthermore, the related research progress into parameter setup and optimization algorithms is also summarized. The remainder of this part is structured as follows. Firstly, we talk about the imaging models. The related models are then described, including the data fidelity and regularization terms. Some advanced techniques and challenges are then discussed, including adaptive parameter setup, blind reconstruction, and optimization strategies.

3.1. The observation model

The imaging model, which refers to the observation model, is essential to SR when using a regularized framework. Before reconstruction, we need to clarify the process by which the observed images have been obtained. The image acquisition process is inevitably confronted with a set of degrading factors, such as optical diffraction, under-sampling, relative motion, and system noise. In general, we usually suppose that the degradation procedure during image acquisition involves warping, blurring, down-sampling, and noise (Fig. 4), and the observation model is simulated as follows:

$$\boldsymbol{y}_k = \boldsymbol{O}_k \boldsymbol{D}_k \boldsymbol{B}_k \boldsymbol{M}_k \boldsymbol{z} + \boldsymbol{n}_k \qquad (1)$$

where there are K LR images participating in the reconstruction. As $N_{1k} \times N_{2k}$ is defined as the size of the kth input LR image, $L_{1k}N_{1k} \times L_{2k}N_{2k}$ is set as the size of the reconstructed HR data, which is determined by the horizontal and vertical magnification factors L_{1k} and L_{2k}. In (1), $\boldsymbol{z}$ is the vector form of the reconstructed image with a size of $L_{1k}N_{1k}L_{2k}N_{2k} \times 1$, which is given as $\boldsymbol{z} = \left[z_1, z_2, \cdots, z_{L_{1k}N_{1k}L_{2k}N_{2k}} \right]^T$, and $\boldsymbol{y}_k = \left[y_{k,1}, y_{k,2}, \cdots, y_{k,N_{1k}N_{2k}} \right]^T$ is the vector form of the kth input dataset. $\boldsymbol{D}_k$ is the down-sampling matrix of size $N_{1k}N_{2k} \times L_{1k}N_{1k}L_{2k}N_{2k}$, $\boldsymbol{B}_k$ represents the blurring operator with size of $L_{1k}N_{1k}L_{2k}N_{2k} \times L_{1k}N_{1k}L_{2k}N_{2k}$, and $\boldsymbol{M}_k$ is the warp matrix describing the motion information (e.g. translation, rotation, etc.). $\boldsymbol{n}_k$ ($N_{1k}N_{2k} \times 1$) indicates the additive noise. $\boldsymbol{O}_k$ is the operator excluding the unobservable pixels from the kth image [47,74,75]. In this way, we can deal with the inpainting and SR problem simultaneously if there are invalid pixels and/or motion outliers in the LR images (Fig. 4).

We can obtain the observation model for single-frame SR when $K = 1$ in (1). If $\boldsymbol{D}_k$ and $\boldsymbol{M}_k$ are excluded, it is a model for image restoration, only dealing with the problems of noise, blurring, or missing information. For convenience of expression, we rewrite

model (1) by substituting the product of $\boldsymbol{O}_k$, $\boldsymbol{D}_k$, $\boldsymbol{B}_k$, and $\boldsymbol{M}_k$ by $\boldsymbol{H}_k$, which is as follows:

$$\boldsymbol{y}_k = \boldsymbol{H}_k \boldsymbol{z} + \boldsymbol{n}_k \qquad (2)$$

The model in (1) is still insufficient for expressing all possible situations. As a result, other models take more complicated factors into consideration to better describe real cases, including different kinds of noise [52,76], dimensional complexity [51], domain transformation for the particular images [77], etc. These models are not discussed in detail in this paper.

3.2. Regularized reconstruction methods

3.2.1. The regularized framework

Based on the observation model described above, the target is to reconstruct the HR image from a set of warped, blurred, noisy, and under-sampled measured images. As the model in (2) is ill-conditioned, SR turns out to be an ill-posed inverse problem. Based on maximum *a posteriori* (MAP) theory, the problem we need to solve can be transformed to the minimization problem as [62,78]

$$E(\boldsymbol{z}) = \arg \min_{\boldsymbol{z}} \sum_{k=1}^{K} \rho(\boldsymbol{y}_k - \boldsymbol{H}_k \boldsymbol{z}) + \lambda U(\boldsymbol{z}) \qquad (3)$$

where $\rho(\cdot)$ and $U(\cdot)$ indicate the corresponding constraint functions. In (3), the first term is the data fidelity term, and the second term is the regularization term, with $U(\boldsymbol{z})$ being the energy function. λ is the regularization parameter balancing these two terms. This is the general variational regularized SR framework. Without the regularization term, this is equal to maximum likelihood (ML) estimation. The MAP methods incorporate the prior constraints of the image, and obtained the results by maximizing the cost function of the posterior probability. They are popular for their flexibility with edge-preserving priors and joint parameter estimation. Comparatively, Bayesian estimation are used when the *posteriori* probability distribution of the unknown parameters, instead of the specific parameters, is estimated.

3.2.2. The data fidelity term

The data fidelity term is used to constrain the residuals between the real LR images and the simulated ones obtained, and it is usually associated with the noise model. For instance, the l_2
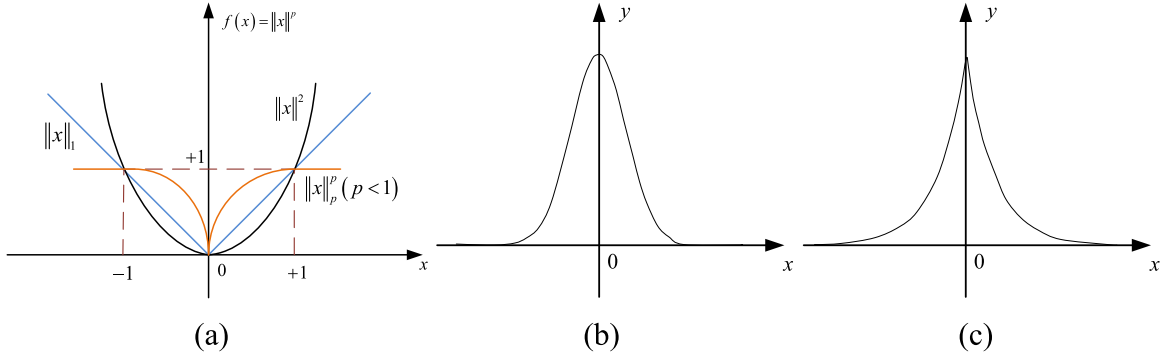
Fig. 5. The properties of different norm functions and the error distribution, where (b) and (c) indicate the distribution for Gaussian and Laplacian errors, respectively. The l_2 norm corresponds the quadratic curve in (a), which is consistent with the Gaussian distribution in (b). In contrast, the plot of l_1 norm is more consistent to the Laplacian distribution.

norm based linear least-squares term is widely used [41,49,62,79,80], as $p = 2$ in (4). The main advantage of the l_2 norm problem is that it is easy to solve, and many efficient algorithms exist [43,81]. However, the result solved by the l_2 model is only optimal when the model error is white-Gaussian distributed [82].
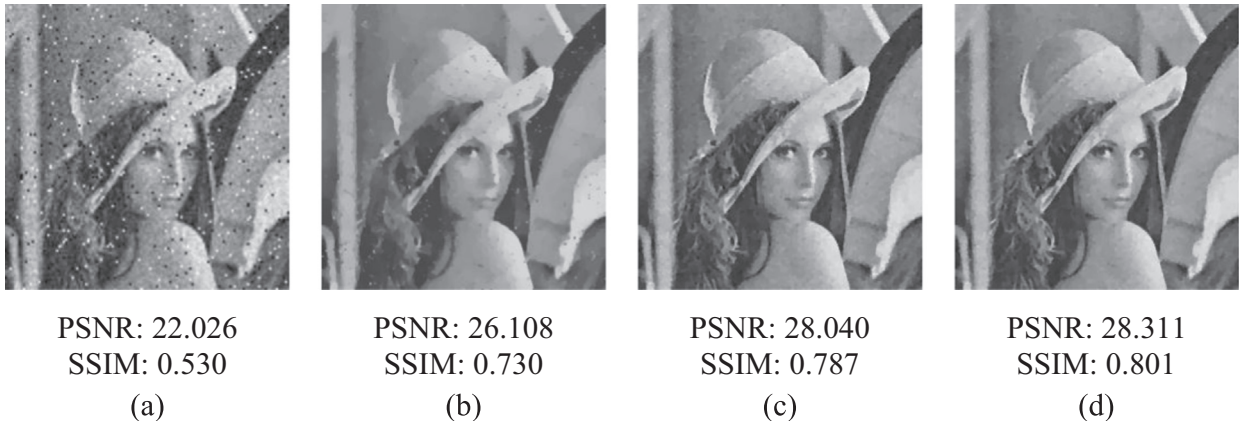
$$F(z) = \sum_{k=1}^{K} \left\| y_k - H_k z \right\|_p^p \tag{4}$$

As a result, there has been a growing interest in choosing the l_1 norm as the function $\rho(\cdot)$ in (4) for image SR and restoration, where $p = 1$ in (4). As the l_2 norm corresponds to Gaussian distributed errors, the l_1 norm mainly corresponds to the Laplacian error model, as shown in Fig. 5. According to Farsiu et al. [43], $p = 1$ results in a pixel-wise median and $p = 2$ leads to a pixel-wise mean of all the measurements after motion compensation in the SR model. It has been proven that the $l_1 - norm$ fidelity is more effective than the $l_2 - norm$ fidelity when the images contain non-Gaussian errors [43,83].
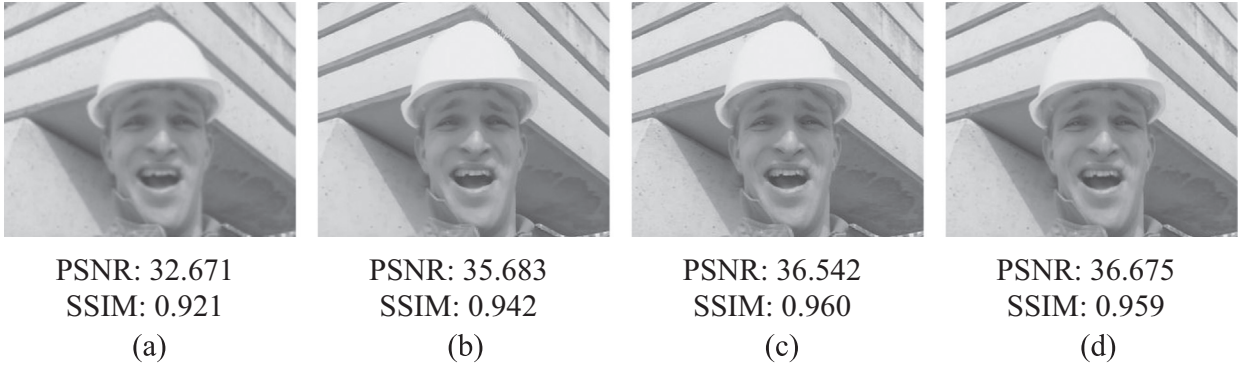
For complicated types of noise and/or model error, however, both the l_1 norm and the l_2 norm have their advantages and disadvantages. Some researchers have therefore employed improved techniques for the data fidelity term [52,81,84–87]. In cases with mixed error modes, the l_p norm function ($1 \leq p \leq 2$) is sometimes employed as the constraint function because of its convex property and its pertinence for the imaging model errors [81]. When $1 \leq p \leq 2$, it results in a weighted mean of measurements. If the value of p is close to one, then the solution is calculated with a larger weight around the measurements near the median value. When the value of p is near to two, the solution is approximated to the average value [43]. In some cases, images are contaminated by

both Gaussian and non-Gaussian errors, and the l_p norm function is considered to be an effective solution [81,82]. According to the imaging model, detecting the outliers and restoring them in matrix O_k as unobservable pixels is also an effective way to exclude the impulse noisy pixels and the motion outliers belonging to non-Gaussian errors [47].

The comparative reconstruction results for the different fidelity norms are given in Figs. 6–7. In the first case, the synthetic test was conducted with the *Lena* test image, in which the original image was first down-sampled by a factor of two in both the horizontal and vertical directions. Thus, four LR images were obtained, with the translational shifts being (0, 0), (0, 0.5), (0.5, 0), and (0.5, 0.5). A mixed mode of Gaussian (normalized variance 0.003) and impulse noise (density 0.03) was then added in the LR images. In the *Foreman* experiment, five degraded images with moving objects were included in the reconstruction, and the 24th frame of the video sequence was set as the reference frame. The LR images were obtained using the corresponding HR frames in the video, with a down-sampling factor of two. We evaluate the results of the synthetic experiments using the peak signal-to-noise ratio (PSNR) and the structural similarity (SSIM) index [88]. The PSNR is used to evaluate the gray value similarity, while the SSIM is mainly employed to reflect the structural similarity [89]. When images are contaminated with mixed noise (Fig. 6), the l_2 norm cannot completely remove the speckles while preserving the texture. In contrast, the l_1 norm has some problems in dealing with Gaussian-distributed noise, and the l_p norm can obtain better results, in terms of both the visual effect and quantitative indexes. In the second test, it can be clearly seen that l_1 and l_p are more robust than l_2 when dealing with motion outliers in the LR observations.

PSNR: 22.026	PSNR: 26.108	PSNR: 28.040	PSNR: 28.311
SSIM: 0.530	SSIM: 0.730	SSIM: 0.787	SSIM: 0.801
(a)	(b)	(c)	(d)

Fig. 6. The SR reconstruction results of the *Lena* image by (a) bilinear interpolation, and (b) MAP with l_2-norm fidelity, (c) l_1-norm fidelity, and (e) l_p-norm fidelity, with $p = 1.3$.

PSNR: 32.671
SSIM: 0.921
(a)

PSNR: 35.683
SSIM: 0.942
(b)

PSNR: 36.542
SSIM: 0.960
(c)

PSNR: 36.675
SSIM: 0.959
(d)

Fig. 7. The SR reconstruction results of the noiseless *Foreman* image by (a) bilinear interpolation, and (b) MAP with l_2-norm fidelity, (c) l_1-norm fidelity, and (e) l_p-norm fidelity, with $p = 1.5$.

With the ability to deal with motion outliers, both l_1 and l_p can prevent the reconstructed details from being oversmooth. Furthermore, the $l_p - norm$ fidelity can achieve a balance between removing noise and suppressing motion artifacts in the noisy cases [52].

A weighted data fidelity term is also suitable for some cases in which the LR images make different contributions to the reconstructed image [25,79,90]. In some practical cases, the amount of available information contained in each LR image might differ according to the image quality (e.g., noise level, spatial resolution, angle, etc.). Thus, different weights should be considered in such cases, as in (5). A weighted data fidelity term has been widely used in the related works, and different methods were presented to determine w_k [25,79,90]. The core idea is to discriminate between the different contributions of the LR images involved in SR.

$$F(\mathbf{z}) = \sum_{k=1}^{K} w_k \cdot \left\| \mathbf{y}_k - \mathbf{H}_k \mathbf{z} \right\|_p^p. \tag{5}$$

3.2.3. The regularization term

The regularization plays a significant role in the regularized variational framework. As SR is a classical ill-posed inverse problem, regularization is therefore adopted to stabilize the inversion process [4,47,91]. According to the Bayesian theorem, the regularization term represents the image prior modeling, providing the prior knowledge about the desired image [4,72,92]. Over the past 10 years of vigorous development, there have been a large amount of studies of regularization for image restoration and SR [81,89,93–98].

3.2.3.1. Smoothness prior models. In the early years, the smoothness of natural images was mainly considered, which leads to the quadratic property of the regularizations [99,100]. Tikhonov-based regularization is the representative smoothing constraint, whose energy function is usually defined as

$$U(\mathbf{z}) = \|\mathbf{\Gamma z}\|_2^2 \tag{6}$$

where $\mathbf{\Gamma}$ is usually chosen as an identity matrix or high-pass operator (e.g., a difference operator or a weighted Fourier operator). Laplacian regularization is one of the most common regularizations used in SR, and was developed from Tikhonov regularization by choosing the smoothing operator as the discrete 2-D operator [100].

Another category of regularization is based on Markov theory. A Markov random field (MRF) assumes that the value of a pixel is only related to the adjacent pixels, which satisfy a Gibbs density function [50]. In this way, MRF can efficiently describe the local statistical characteristics of images. The energy function can be given as

$$U(\mathbf{z}) = \sum_{c \in C} V_c(\mathbf{z}) = \sum_{t=1}^{\tau} \phi\left(d_c^t \mathbf{z} \right) \tag{7}$$

where d_c^t is a coefficient vector for clique c, which is usually defined as the finite-difference approximations to second-order derivatives in the four directions. $\phi(\cdot)$ is the constraint function. The regularization function is usually divided into two categories, Gaussian MRF (GMRF) [78] or Huber MRF (HMRF) [101], in accordance with the choice of $\phi(\cdot)$. For GMRF regularization, the quadratic l_2 norm is employed for $\phi(\cdot)$.

These regularized methods smooth the restored image by penalizing the high-frequency component, and thus perform well in suppressing noise. However, they inevitably oversmooth the sharp edges and detailed information.

3.2.3.2. Edge-preserving prior models. The smoothing prior models are somewhat against the nature of images, in that sharp details in images are always desirable for human beings in many applications, including remote sensing imaging, medical diagnosis and object recognition [2,28,69]. Thus, $l_1 - norm$ based regularizations are often preferred for their edge-preserving properties [93,101,102]. The representative total variation (TV) regularization was first proposed by Osher et al. [93,103], based on the fact that an image is naturally "blocky" and discontinuous. The standard TV norm is given as

$$U(\mathbf{z}) = \sqrt{(\nabla^h \mathbf{z})^2 + (\nabla^v \mathbf{z})^2 + \beta} \tag{8}$$

where $\nabla^h \mathbf{z}$ and $\nabla^v \mathbf{z}$ are the first-order image gradients in the horizontal and vertical directions, respectively. Here, β is a small scalar to ensure differentiability.

Unlike the quadratic regularizations, edge information can be better preserved using TV regularization, with the l_1 norm to deal with the image information rather than the l_2 norm [47,104,105]. Therefore, the TV prior model has been the most popular model for image processing in the last two decades, and has been applied in fields such as image denoising, deblurring, segmentation, and SR [47,76,104,106]. However, the results of the TV prior model will often result in a "staircase" effect with strong noises, especially in flat regions [89].

To overcome the shortcomings of the TV prior model, some researchers have proposed spatially adaptive strategies. A number of methods use spatially adaptive regularization parameters to eliminate the staircase effects [94,107–109]. Some of them classified the image into detailed and flat regions using the spatial information, and used a larger penalty parameter for the flat regions and a smaller one for the edges [94,107]. However, the spatially adaptive indicators such as gradients, the difference curvature, and

structure tensor are usually sensitive to noise.

Moreover, different norm constraints can also be employed for the prior modeling in a spatially adaptive way [96,108]. The l_p norm, rather than the l_1 norm, can be used as the constraint function for ∇z in the TV term. As the l_2 norm represents a smoothing prior and the l_1 norm tends to preserve the edges, the l_p ($1 \le p \le 2$) norm achieves a balance between them, thereby avoiding the staircase effect [110]. Other improvements include higher-order TV (HDTV) [111], bilateral TV (BTV) [43], locally adaptive BTV (LABTV) [96], etc.

HMRF is also a representative edge-preserving prior model [101,112]. A hybrid norm can theoretically achieve a balance between preserving edges and suppressing noise, to some degree. For the HMRF term, $\phi(\cdot)$ in (7) is chosen as the Huber function, which is piecewise as:

$$\phi(x) = \begin{cases} x^2 & x \le T \\ 2T|x| - T^2 & x > T \end{cases} \tag{9}$$

where T is the threshold. The Huber function satisfies the properties of convexity, symmetry, and discontinuity. The HMRF model is effective when dealing with images with clear texture. However, only the neighborhood information is considered, which limited its performance [113].

3.2.3.3. Nonlocal-based priors. The local derivatives are somewhat sensitive to noise in the images' homogenous regions, which negatively affects the reconstruction effect in noisy cases. Recently, the concept of nonlocal-based priors has been proposed and has developed rapidly in image processing [97,114–116]. Rather than defining the neighborhood of a pixel locally, nonlocal-based priors consider pixels in a large search area and weight them according to the similarity between rectangular patches. This is based on the assumption that every feature in a natural image can be found many times in the same scene [114]. The nonlocal models have become popular in the regularized framework, given the nonlocal TV regularization as
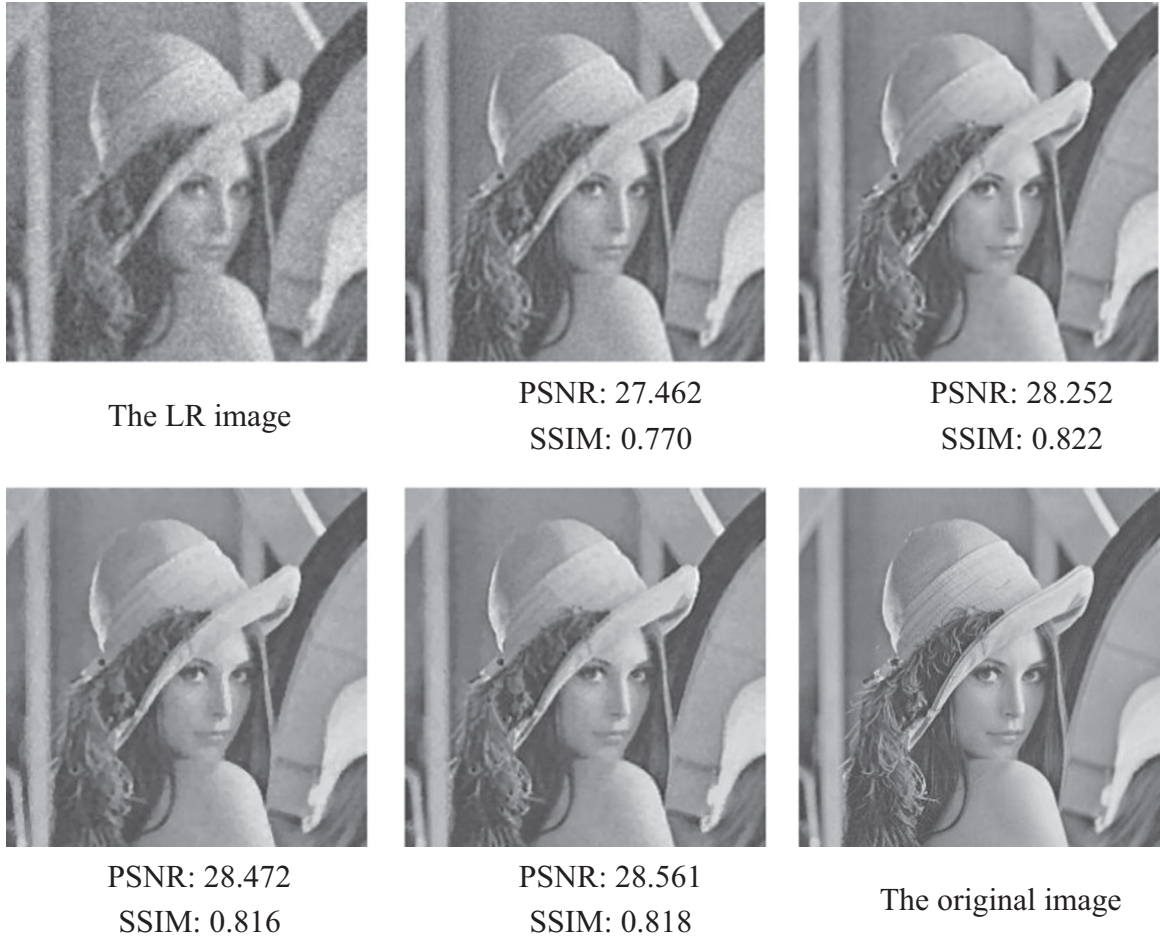
$$U_{NLTV}(\mathbf{z}) = \sum_{i \in \Omega} \sum_{j \in \Pi_i} w(i,j) \big| \mathbf{z}(i) - \mathbf{z}(j) \big| \tag{10}$$

where i indicates one of the pixels in the image $\mathbf{z} : \Omega \to \mathbb{R}$, and the search window is usually restricted to the square neighborhood of i, denoted as Π_i. The weight function $w(i,j)$ can then be defined as

$$w(i,j) = \exp\left(-\frac{\|P_i(\mathbf{z}) - P_j(\mathbf{z})\|_p^p}{\sigma^2} \right) \tag{11}$$

Here, $P_i(\mathbf{z})$ and $P_j(\mathbf{z})$ represent the $(2n+1) \times (2n+1)$ patch of $\mathbf{z}$, centered at the pixel i (or j) with a radius of n. The similarity can be calculated with various distance formulas (e.g., by choosing different values of p). σ is the filtering parameter. Compared with the TV model, the nonlocal-based model can make use of more information, and can thus prevent the staircase effect in flat regions, and can help restore the details [97,113].

The comparative results of the typical regularizations are displayed in Fig. 8. The down-sampling process was set the same as for the *Lena* image in Section 3.2.2. The generated LR images were then blurred by a 3*3 filter with a variance of 1, and contaminated

<table>
<tr><td align="center">The LR image</td><td align="center">PSNR: 27.462
SSIM: 0.770</td><td align="center">PSNR: 28.252
SSIM: 0.822</td></tr>
<tr><td align="center">PSNR: 28.472
SSIM: 0.816</td><td align="center">PSNR: 28.561
SSIM: 0.818</td><td align="center">The original image</td></tr>
</table>

Fig. 8. The SR reconstruction results using different regularizations. Top row: bilinear interpolation, Laplacian regularization, and HMRF regularization [100]. Bottom row: TV regularization [47], NLTV regularization [114], and the original HR image.

by Gaussian noise with a standard variance of 10. From the results, it can be seen that all the edge-preserving regularizations perform well in removing noise and preserving the details. Nevertheless, the results of the HMRF and nonlocal TV models better conform to human visual perception.

In addition to the above regularizations, there have been many other studies of prior models, such as regularization based on sparsity [117], along with morphological theory [98]. The common goal of all these methods is that they want to reconstruct a noiseless HR image with natural texture and clear, detailed information. There have also been studies of spectral images (e.g., digital color images or hyperspectral images), where the emphasis has been on the preservation of spectral information, while enhancing the spatial resolution [118,119].

3.2.4. Adaptive regularization parameter selection

Parameter selection is always a headache when dealing with ill-posed inverse problems. The regularization parameter, in particular, plays a significant role in image SR. In this part, we present the main approaches to adaptive strategies for determining the regularization parameter λ in (6).

In many cases, the regularization parameter is selected manually. The common approach is to test a sequence of regularization parameters and select the optimal parameter corresponding to the best results evaluated by quantitative indexes or visual inspection. This is, however, a time-consuming and subjective process. Therefore, adaptive strategies are necessary in the SR process. A number of strategies have been specially designed to adaptively estimate the regularization parameter. These strategies have mainly been inspired by developments in the inverse problem field, such as denoising and deblurring [120–123]. The popular methods include the L-curve method [124], generalized cross-validation (GCV) [35], and the U-curve method [49].

It has been noted in the earlier studies that the GCV method tends to give unsatisfactory results if the model errors are highly correlated [121]. The L-curve method has some advantages over GCV, including well-defined numerical properties and robustness in dealing with highly correlated errors. Both of the L-curve and U-curve methods are based on the parametric plots generated by varying the regularization parameter λ. The target is to find the optimal λ that achieves a good balance between minimizing the data fidelity and regularization. As the $l_2 - norm$ based model is chosen, the energy function can be given as

$$E(\mathbf{z}) = \arg \min_{\mathbf{z}} \sum_{k=1}^{K} \left\| \mathbf{y}_k - \mathbf{H}_k \mathbf{z} \right\|^2 + \lambda \|\mathbf{\Gamma} \mathbf{z}\|^2 \tag{12}$$

where $\mathbf{\Gamma}$ indicates the two-dimensional Laplacian operator. After using the singular value decomposition (SVD) least-squares method for $\mathbf{H}_k$, we define

$$R(\lambda) = \sum_{k=1}^{K} \|\mathbf{y}_k - \mathbf{H}_k \hat{\mathbf{z}}_\lambda\|^2, \ P(\lambda) = \|\mathbf{\Gamma} \hat{\mathbf{z}}_\lambda\|^2 \tag{13}$$

The L-curve method searches for the distinct L-shaped corner using the relationship between $R(\lambda)$ and $P(\lambda)$, while the U-curve method selects the maximum curvature point close to the left vertical part of the U-curve ($U(\lambda) = \frac{1}{R(\lambda)} + \frac{1}{P(\lambda)}$) as the optimal parameter. It has been proved that the U-curve method can obtain more accurate solutions in quadratic cases for SR. Further details can be found in the related works [49,124]. These methods can obtain relatively good solutions, but they have not yet been extended to the general regularized framework with various regularizations.

It has to be mentioned that the Bayesian framework [53,72] is also a powerful tool for modeling unknown parameters, including

the regularization parameter, the blur kernel, and motion vectors. We discuss the Bayesian methods in the next section.

3.2.5. Blind reconstruction

Earlier in this article, we have discussed the main developments in the SR framework based on MAP theory, from the point of view of data fidelity and regularization. However, the techniques mentioned before are used with the assumption that the parameters, such as the motion model, blur kernel, and noise level, are known [62]. This is impractical in real-world cases, where the motion of objects and cameras cannot be estimated beforehand. In addition, the point spread functions (PSFs) and the noise level are always unknown.

The traditional methods deal with parameter estimation and reconstruction separately. These methods regard registration and blur kernel identification as a preprocessing stage [43,79,96]. However, the parameters estimated using only the LR images can be inaccurate, which will lead to an unsatisfactory performance. We introduce two effective strategies for blind reconstruction below.

3.2.5.1. The joint MAP framework. The MAP framework is advantageous in parameter estimation due to its flexibility in adding priors for the unknown parameters [4]. Therefore, some researchers have developed joint MAP methods to adaptively obtain the unknown parameters [62,125,126]. Similar to the observation model in (1), we define the LR observations as $\mathbf{y} = \left[\mathbf{y}_1^T, \mathbf{y}_2^T, \cdots, \mathbf{y}_K^T \right]^T$, the motion vectors as $\mathbf{s} = \left[\mathbf{s}_1^T, \mathbf{s}_2^T, \cdots, \mathbf{s}_K^T \right]^T$, and the PSFs as $\mathbf{h} = \left[\mathbf{h}_1^T, \mathbf{h}_2^T, \cdots, \mathbf{h}_K^T \right]^T$. The observation model in (1) can then be expressed in matrix notation as (14)

$$\mathbf{y} = \mathbf{ODB}(\mathbf{h})\mathbf{M}(\mathbf{s})\mathbf{z} + \mathbf{n} \tag{14}$$

Noting that $\mathbf{z}$, $\mathbf{h}$, and $\mathbf{s}$ are statistically independent, we can form an estimate of the unknown parameters simultaneously, according to the theory of MAP. Once we determine the probability density function (PDF) of $\mathbf{z}$, $\mathbf{h}$, and $\mathbf{s}$, the ill-posed inverse problem can be solved by optimizing the following cost function:

$$\hat{\mathbf{z}}, \hat{\mathbf{h}}, \hat{\mathbf{s}}$$
$$= \arg \min_{\mathbf{z}, \mathbf{h}, \mathbf{s}} \left\{ \|\mathbf{y} - \mathbf{ODB}(\mathbf{h})\mathbf{M}(\mathbf{s})\mathbf{z}\|_p^p + \lambda_1 U(\mathbf{z}) + \lambda_2 U(\mathbf{h}) \right.$$
$$\left. + \lambda_3 U(\mathbf{s}) \right\} \tag{15}$$

The estimated parameters are iteratively updated along with the reconstructed image in a cyclic optimization procedure. However, there will be a number of unknown parameters which need to be tuned.

3.2.5.2. The Bayesian framework. Differing from the MAP estimator, the Bayesian methods calculate the posterior distribution instead of setting specific values of the parameters for the SR system [72,127]. Both the ML and MAP estimators return only single and specific values for the parameters, while Bayesian estimation, in contrast, fully calculates the posterior distribution $p(\mathbf{z}, \mathbf{h}, \mathbf{s}|\mathbf{y})$.

The Bayesian inference is based on the posterior distribution, and thus

$$p(\mathbf{z}, \mathbf{h}, \mathbf{s}|\mathbf{y}) = \frac{p(\mathbf{z}, \mathbf{h}, \mathbf{s}, \mathbf{y})}{p(\mathbf{y})} \tag{16}$$

Here $p(\mathbf{z}, \mathbf{h}, \mathbf{s}, \mathbf{y})$ refers to $p(\mathbf{y}|\mathbf{z}, \mathbf{h}, \mathbf{s})p(\mathbf{z})p(\mathbf{h})p(\mathbf{s})$ for the convenience of expression. $p(\mathbf{y})$ is independent of the unknown variables, and is usually ignored in the MAP estimator. In fact, as in many applications, $p(\mathbf{z}, \mathbf{h}, \mathbf{s}|\mathbf{y})$ is intractable because $p(\mathbf{y})$ cannot be computed [72]. Approximation methods need to be utilized for the reconstruction [45,53,72]. In Babacan's work [72], they utilized

a variational Bayesian method by minimizing the Kullback–Leibler (KL) distance between the posterior $p(z, h, s|y)$ and a tractable distribution $q(z, h, s)$. Assuming the approximated distribution $q(z, h, s)$ can be factorized, the distribution of the corresponding parameter can be estimated by calculating the corresponding expectation using the first-order Taylor series.

By estimating the full posterior distribution of the unknowns instead of point estimations corresponding to the maximum probability (e.g., MAP), the uncertainty of the estimates is incorporated into the estimation procedure. In addition, the unknown parameters can be estimated during the iterative estimation process [41,53,72]. Nevertheless, the accuracy of the Bayesian framework depends on the parameter distribution models, and is influenced by some attached parameters via the iterations.

3.2.6. Optimization methods

After the reconstruction model is built, the HR image can be acquired by optimizing the corresponding cost function. If a Gaussian distribution is chosen for the noise model, and a quadratic constraint is employed for the regularization, then the energy function can be given as (12). The Euler–Lagrange function can be acquired as follows:

$$\nabla E(z) = -\sum_{k=1}^{K} H_k^T (y_k - H_k z) + \lambda \Gamma^T \Gamma z = 0 \tag{17}$$

For the quadratic equation, z^{n+1} can be obtained as the solution to the linear equation

$$\left[\sum_{k=1}^{K} H_k^T H_k - \Gamma^T \Gamma\right] z^{n+1} = \sum_{k=1}^{K} H_k^T y_k \tag{18}$$

The minimization of the standard $l_2 - norm$ based model is the regularized solution of a linear partial differential equation (PDE). To solve this quadratic ill-posed inverse problem, a conjugate gradient (CG) or preconditioned CG (PCG) method is usually employed to optimize the Lagrangian functional [47,128]. With the initial estimation and stopping criterion for the iteration given, the estimated result will approximate the numerical solution via iterations.

However, the l_2 norm-based model cannot acquire satisfactory results in many real cases. Compared with the l_2 norm, it is difficult to employ conventional numerical methods for $l_1 - norm$ problems directly, due to the nonlinearity of the l_1 norm function. Moreover, the convergence rate cannot meet the demand of large-scale inverse problems. Some efficient approximation methods have been developed for optimizing the l_1 norm regularized functional [102,104,105,128–131]. Typically, the popular numerical algorithms for the nonlinear SR problems can be roughly classified into two categories, which are: (1) Euler–Lagrange smooth approximation; and (2) primal–dual/splitting algorithms.

3.2.6.1. Euler–Lagrange smooth approximation.
As we know, perfect or exact solutions are often difficult to acquire. The common goal is to find the optimal solution in a statistical sense. Euler–Lagrange smooth approximation methods generally use a smooth approximation of the $l_1 - norm$, thus construct a linear functional to optimize. The representative algorithms include lagged diffusivity fixed point iteration (LDFPI) [128], majorization-minimization (MM) [104], the iteratively reweighted norm (IRN) [129,132], and the half-quadratic algorithm [95]. As one of the most popular regularizations employed in image restoration, the TV model is a classical non-quadratic optimization problem. Here, we take the $l_2 - TV$ SR model as an example to show the specific approximation process. The notations are based on LDFPI [128] and IRN [129], respectively. The reconstruction model can be given as

$$\hat{z} = \arg\min_z \left\{ \sum_k^K \|y_k - H_k z\|_2^2 + \lambda \|\nabla z\|_{TV} \right\} \tag{19}$$

where $\|\nabla z\|_{TV}$ indicates the isotropic TV regularization defined in (8). The Euler–Lagrange equation for the energy function in (19) is given by the following nonlinear system:

$$\nabla E(z) = \sum_k H_k^T (H_k z - y_k) - \lambda L_z z = 0 \tag{20}$$

where $L_z = \nabla \cdot \left(\nabla / \sqrt{|\nabla z|^2 + \beta}\right)$, which is the matrix form of a central difference approximation of the differential operator, with $\nabla \cdot$ being the divergence operator. This is a nonlinear equation for z. To transform the functional to a linear PDE, smooth approximation strategies need to be adopted. LDFPI, which was first introduced by Vogel [128], linearizes the differential term by lagging the diffusion coefficient $1/\sqrt{|\nabla z|^2 + \beta}$ one iteration behind. Thus z^{n+1} is obtained as the solution to the approximated linear equation

$$\left[\sum_k H_k^T H_k - \lambda L_z^n\right] z^{n+1} = \sum_k H_k^T y_k \tag{21}$$

Usually, half-point discretization [133] is used to approximate L_z^n. To solve the linear PDE above, a CG or PCG method is desirable. IRN is a method which can minimize the l_p norm ($p \le 2$) by approximating it with a weighted l_2 norm [129].

$$\|u\|_p^p = \sum_k \left(|u_k|^{p-2}\right) u_k^2 = \sum_k w_k u_k^2 = u^T W u = \|W^{1/2} u\|_2^2 \tag{22}$$

where $W = diag\left(|u|^{p-2}\right)$. Introducing the idea into the energy function in (22), the functional can be expressed as

$$z = \arg\min_z \left\{ \sum_k^K \|y_k - H_k z\|_2^2 + \frac{\lambda}{2} \left\|\tilde{W}_R^{1/2} \nabla z\right\|_2^2 \right\} \tag{23}$$

where

$$\tilde{W}_R = \begin{pmatrix} W_R & 0 \\ 0 & W_R \end{pmatrix} \tag{24}$$

Here, we define

$$W_R = diag\left(2f_R\left((\nabla_h z)^2 + (\nabla_v z)^2\right)\right) \tag{25}$$

where the constraint function $f_R(x) = \begin{cases} |x|^{-1/2} & if |x| > \varepsilon \\ 0 & f|x| \le \varepsilon \end{cases}$. Thus, the Euler–Lagrange function can be linearized as

$$\left[\sum_k H_k^T H_k - \lambda \nabla^T \tilde{W}_R^n \nabla\right] z^{n+1} = \sum_k H_k^T y_k \tag{26}$$

The weight matrix $\tilde{W}_R^n$ can by calculated by (23)–(25) using z^n. It appears that LDFPI and IRN are two different methods; however, they are almost the same in essence when dealing with the $l_1 - norm$ problem by smooth approximation. In fact, all the algorithms mentioned above obtain similar results with TV minimization, including LDFPI, IRN, MM, and the half-quadratic algorithm, where lagged iteration was used. Consequently, they can be inferred from each other by transformation. This category of methods is simple to implement, and can be extended to deal with the regularized inversions with various norms.

3.2.6.2. Primal–dual/splitting algorithms.
The second group of methods split the original optimization task into a primal problem and a dual formulation of this problem. In recent years, abundant

related studies have been presented, such as the alternating direction method of multipliers (ADMM) [131,134], the primal–dual (PD) based algorithms [105], the Douglas-Rachford algorithm [135], proximal forward backward splitting (PFBS) [130], and the split-Bregman (SB) method [102]. ADMM is one of the most prevalent methods for convex optimization in image processing. It converts the optimization of the original nonlinear problem into looking for a saddle point of an augmented version of the classical Lagrange function [131]. Given the original model as (19), it can be expressed as the following with an auxiliary variable $\boldsymbol{b}$ introduced

$$\arg \min_{\boldsymbol{z},\boldsymbol{b}} \left\{ \frac{1}{2} \sum_k \|\boldsymbol{y}_k - \boldsymbol{H}_k \boldsymbol{z}\|_2^2 + \lambda \|\boldsymbol{b}\|_1 \right\} \ s.\,t.\ \nabla \boldsymbol{z} = \boldsymbol{b} \tag{27}$$

To transform (27) to generate an unconstrained problem, the *augmented Lagrangian* can be rewritten as

$$\mathcal{L}_\tau(\boldsymbol{z}, \boldsymbol{b}, \boldsymbol{u}) = \left\{ \frac{1}{2} \sum_k \|\boldsymbol{y}_k - \boldsymbol{H}_k \boldsymbol{z}\|_2^2 + \tau \boldsymbol{u}^T (\nabla \boldsymbol{z} - \boldsymbol{b}) + \frac{\tau}{2} \|\nabla \boldsymbol{z} - \boldsymbol{b}\|_2^2 + \lambda \|\boldsymbol{b}\|_1 \right\} \tag{28}$$

where $\boldsymbol{u}$ is the introduced as *Lagrangian multiplier*, and $\tau > 0$ is the penalty parameter. It is easy to minimize the objective function in (28) with respect to either $\boldsymbol{z}$ or $\boldsymbol{b}$. The optimization expression can be given by (29)

$$\boldsymbol{z}^{n+1} := \left(\sum_k \boldsymbol{H}_k^T \boldsymbol{H}_k - \tau \nabla^T \nabla \right)^{-1} \left(\sum_k \boldsymbol{H}_k^T \boldsymbol{y}_k + \tau \nabla^T \left(\boldsymbol{b}^k - \boldsymbol{u}^k \right) \right)$$

$$\boldsymbol{b}^{n+1} := S_{\lambda/\tau} \left(\nabla \boldsymbol{z}^{n+1} + \boldsymbol{u}^n \right)$$

$$\boldsymbol{u}^{n+1} := \boldsymbol{u}^n + \left(\nabla \boldsymbol{z}^{n+1} - \boldsymbol{b}^{n+1} \right) \tag{29}$$

For a fixed $\boldsymbol{b}$, it turns out to be a quadratic functional for the variable $\boldsymbol{z}$. The generalized shrinkage formula in the second formula is usually employed to solve the minimization problem for $\boldsymbol{b}^{n+1}$. Finally, the residual term is added to refine the optimization process. Through the alternating iterations, the variables can finally converge to the solution of the original model [131]. The model can be easily extended to more complex models, e.g., a non-quadratic functional with an $l_1 - norm$ data fidelity term.

The relationships between these methods have been discussed in detail in [136]. The Bregman iterative regularization method, the Douglas-Rachford algorithm, and ADMM have been shown to be equivalent under the assumption of linear constraints [136,137]. The most promising aspect of these methods is that by splitting the original large-scale inverse problem into several sub-problems, the computational efficiency can be greatly improved. In general, the PD-based methods are faster than the optimization algorithms based on smooth approximation.

There are also other fast and robust optimization methods for image SR. For example, graph-cut based methods can be applied for the minimization of graph-based energy functions [138,139].

3.3. The main challenges for image super-resolution

Although SR techniques have been developed for three decades, there are some pivotal difficulties. In this section, the main challenges for image SR and the corresponding strategies to deal with these issues are discussed. The challenges are: (1) SR with complex motion conditions; (2) SR without multiple LR images; and (3) acceleration strategies for "big data" processing.

3.3.1. Super-resolution with complex motion conditions

It is a big challenge to achieve accurate motion estimation in complex motion conditions. As a result, the performance of the reconstruction-based SR algorithms is significantly affected. Researchers have therefore attempted to deal with the problems brought about by inaccurate motion registration. The solutions include more advanced registration strategies, robust fidelity models, joint parameter estimation, and methods without explicit motion estimation.

3.3.1.1. Advanced registration strategies. In simulated cases, the sub-pixel motion fields between the reference frame and the other frames can be described by a parameter model (e.g., pure translation or global affine warp). However, they have to be estimated point-wise or block-wise under most practical cases with more complicated motion conditions. Optical flow estimation [140] is one of the representative methods to obtain a relatively accurate motion field of all the points. However, the optical flow based methods are computationally expensive [141] and are sensitive to noise, large displacements, and illumination variation [142]. To increase the accuracy of motion estimation in SR, advanced registration methods are necessary. Baboulaz and Dragotti [143] proposed an advanced method to extract features in LR images for registration by taking a sampling perspective. Su et al. [144] attempted to avoid inaccurate flow estimation by accurately estimating the local flow, based on the sparse feature point correspondences.

3.3.1.2. Robust fidelity models. Although more accurate registration methods have been applied, motion errors are inevitable in real cases. Researchers have therefore tried to overcome the influence of inaccurate registration from the perspective of model construction. The effects of the registration error are mainly embodied in the data fidelity term, which provides a constraint for the conformance of the reconstructed HR image to the observed LR image. As mentioned in Section 3.2.2, the l_1 norm performs more robustly in dealing with registration errors than the l_2 norm [43]. Thus, $l_1 - norm$ based SR methods can effectively overcome the influence of motion errors. In addition, as expressed in (5), LR images with a large registration error will make less contribution in the reconstruction process by importing the adaptive channel function w_k [145]. The weight w_k is usually set as inversely proportional to $\|\boldsymbol{y}_k - \boldsymbol{H}_k \boldsymbol{z}\|_p^p$ ($1 \le p \le 2$), and thus reduces the effect of model errors. However, both the $l_1 - norm$ based and weighted models need an extra registration method for motion estimation. Furthermore, the relatively poor convergence performance limits their application.

3.3.1.3. Joint parameter estimation. One of the most popular strategies for improving the reconstruction performance is the joint methods. These approaches (discussed in Section 3.2.5) can obtain better registration results and exclude errors during the iteration by simultaneously estimating the motion parameters and the reconstruction result. Specifically, Tom and Katsaggelos [146] developed a simultaneous registration and reconstruction approach where they formulated the SR problem in the ML framework, and solved it using an expectation-maximization algorithm. Hardie et al. [100] combined a joint approach and a MAP framework to reconstruct the HR image.

The common assumption is that the blur kernel is known in the reconstruction system. The ill-posed inverse problem can be solved by selecting the appropriate PDF of $\boldsymbol{z}$ and $\boldsymbol{s}$. The choice of prior model $U(\boldsymbol{z})$ and $U(\boldsymbol{s})$ in (15) should accurately describe the characteristics of the realization. However, it is a difficult task to determine the regularized constraint of $\boldsymbol{s}$, which is related to the motion model, and it is usually set as constant with a global motion model. If there is more complicated motion, different strategies could be adopted. Shen et al. [62] proposed a joint method combining motion estimation, object-based segmentation, and SR. This method can handle the SR problem with multiple moving objects by iteratively updating the motion fields, segmentation fields, and the HR image. He et al. [126] proposed a nonlinear

least-squares technique for motion models, including both translation and rotation. Furthermore, Tian and Yap [147] proposed a method for SR with a zooming motion and employed $\|\boldsymbol{s} - \bar{\boldsymbol{s}}\|^2$ as the PDF of $p(\boldsymbol{s})$, where $\bar{\boldsymbol{s}}$ is the initial estimate of the motion vectors. Overall, joint super-resolution is an effective way to undertake SR without accurate registration. However, relatively complex models and extra parameters mean that the methods have not been widely applied. Of course, Bayesian methods can also prevent the propagation of estimation errors for the motion fields [53,72].

3.3.1.4. Super-resolution without explicit motion estimation. In recent years, SR methods without explicit motion estimation have become popular. The motivation behind these methods is to seek an SR algorithm that is able to process sequences with a general motion pattern. Protter et al. [148] generalized the nonlocal-means (NLM) algorithm to perform SR reconstruction. Rather than calculating the data fidelity globally, the method divides both the LR images and the estimated HR image into patches to accumulate the weighted residuals of the similar patches. By constructing a penalty function combining fuzzy motion estimation and a patch-based approach, it allows the algorithm to handle diverse motion models. Following this work, Takeda et al. [54] adapted kernel regression to multi-frame SR, and this method is able to handle video sequences with general motion models. Protter and Elad [113] presented a new framework in which the pixel-wise motion field in each pair of images is replaced with a probabilistic motion field. One of the main concerns about SR methods without explicit motion estimation is the computational efficiency, since most of them adopt a patch-based manner and require iteration to obtain the final result.

3.3.2. Super-resolution without multiple low-resolution images

The goal of SR is to recover the HR details which are unobservable in the LR images. Usually, the details are recovered by combining the information across multiple LR images. However, in the real world, sufficient images with supplementary information are sometimes difficult to acquire. The performance of the reconstruction-based algorithms degrades when the magnification factor is large. Thus, researchers have turned to study SR methods for use with a single image, where the observation model is similar to (1) as $K = 1$.

Single-frame SR should not be confused with similar techniques, such as image interpolation and reconstruction methods using little extra information. The high-frequency details cannot be reconstructed without supplementary information. For example, the reconstruction-based methods [91,149–154] involve image priors to "hallucinate" information lost during the image acquisition. Differing from the priors commonly used in multi-frame SR, the single-frame priors are typically designed to reduce edge artifacts and estimate the HR details with little additional external information. Although the edge-preserving operators can remove the ringing artifacts in image resolution enhancement, the main deficiency with mid-frequency textures prevents the methods being effective when the magnification factor is large [11]. In other words, these approaches cannot satisfy our everyday requirements, because of the limited information involved in the reconstruction model. Consequently, we do not regard traditional interpolation and reconstruction-based methods as SR in this review.

Distinguished from the traditional interpolation methods, single-frame SR learns the correspondence between the low- and high-resolution information from an external database, and thus restores the details in the HR space. As with the rapid developments in machine learning, much attention has been paid to example-based SR in recent years. The example-based algorithms [11,12,155–159] either exploit the internal similarities of the same image, or learn the correspondences between the LR and HR image patches from external low- and high-resolution exemplar pairs. In the early stage, patch or feature-based approaches were used to learn the generic relationship between the LR and HR image details [12,160,161]. As a representative work, Freeman et al. [12] employed an MRF framework to learn the prediction from LR to HR images. However, these methods are usually computationally expensive and depend on the similarity between the training set and the test set. As a result, neighbor embedding (NE) methods and sparse coding methods have since been proposed.

The NE-based approaches assume that the small patches in the HR and LR images form similar manifolds in two distinct feature spaces [155–157,162,163]. Chang et al. introduced locally linear embedding (LLE) [155] to predict the HR patch as a linear combination of nearest neighbors from the training dataset, via learning the mapping relationship from the LR to HR space. In this way, the NE-based methods require fewer training samples and can be applied to a variety of images. However, the crucial problems of the NE-based methods are the blurring effects due to over- or under-fitting with the strictly fixed neighborhood size. Moreover, the LR-HR feature mappings cannot be effectively established through learning high-resolution information from the low-dimensional space.

To overcome the limitations, sparse coding (SC) approaches [11,159,164–166] attempt to incorporate sparse signal representation to form a learned overcomplete dictionary, and have obtained quite promising results. Supposing that the image can be represented as a sparse linear combination with an overcomplete dictionary ψ and the corresponding coefficient vector α with very few nonzero entries, then the image patch can be given as $\boldsymbol{x} = \psi\alpha$. In the concept of SR, for each input LR patch $\boldsymbol{y}_r$, the sparse representation will be found with respect to ψ_l, and the HR patch $\boldsymbol{z}_r$ can be generated according to the HR dictionary ψ_h and the coefficients. The target is to find the sparsest representation of α and the corresponding HR image by optimizing the energy function. The unified framework [11] can be interpreted as

$$\hat{\boldsymbol{z}} = \arg\min_{\boldsymbol{z},\{\alpha_{i,j}\}}\left\{\|\boldsymbol{DBz} - \boldsymbol{y}\|_2^2 + \beta\sum_{i,j}\|\psi_h\alpha_{i,j} - P_{i,j}\boldsymbol{z}\|_2^2 + \tau U(\boldsymbol{z}) + \lambda R(\alpha)\right\} \tag{30}$$

where $\alpha_{i,j}$ denotes the representation coefficients for the (i, j)th patch of $\boldsymbol{z}$, α denotes the concatenation of all $\alpha_{i,j}$, and $P_{i,j}$ is a projection matrix which selects the (i, j)th patch from $\boldsymbol{z}$. The $U(\boldsymbol{z})$ indicates the prior term for the reconstructed image, as discussed in Section 3.2.3. By tuning λ and β, the model is able to control the tradeoff between matching the LR input and finding a HR patch which is compatible with its neighbors. In addition, τ can achieve the goal of simultaneously suppressing the noise.

The main advances since then include different training approaches for the dictionary pair [159,166,167], efficiency improvements [168], and various coding strategies [164,169]. In the work of Yang et al. [11], the coefficient α is assumed to be the same with respect to both the LR and HR dictionaries. However, further studies claimed that the differences and connections between the coefficients for the dictionaries should not be ignored [166,170]. This is another tough task for single-image SR based on sparse representation. Other researchers have developed regression-based methods and some improved algorithms, such as the SR method with sparse NE [156], image SR using nonlocal autoregressive modeling [159], and anchored neighborhood regression [171] for fast example-based SR. Recently, Dong et al. [172] presented the sparse coding based SR method, which can also be viewed as a kind of convolutional neural network with a different nonlinear mapping, and applied deep learning to learn an end-to-end mapping between the LR and HR images.
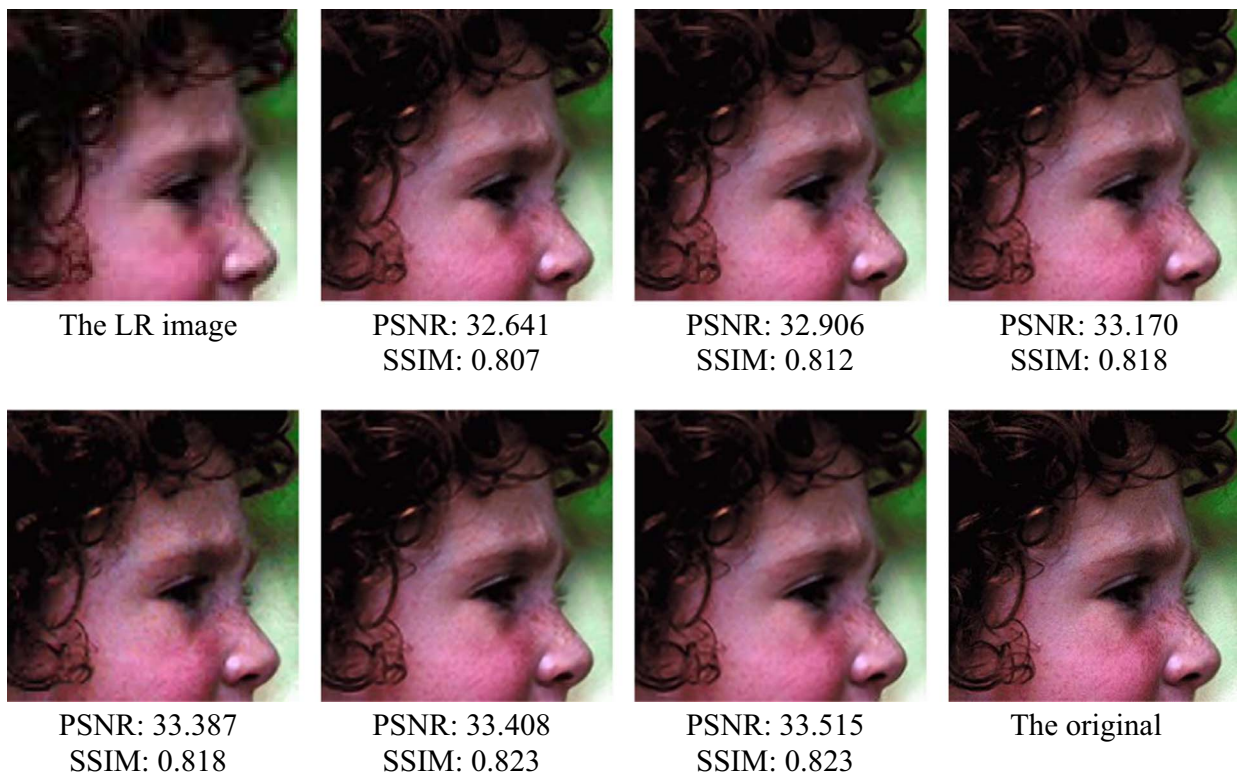
Fig. 9. Results for the *Girl* image with a magnification factor of 3. Top row: The LR image, NE [156], the TV-based method [47], and SC [11]. Bottom row: ASDS-AR-NL [159], SRCNN [172], SPM [166], and the original image.
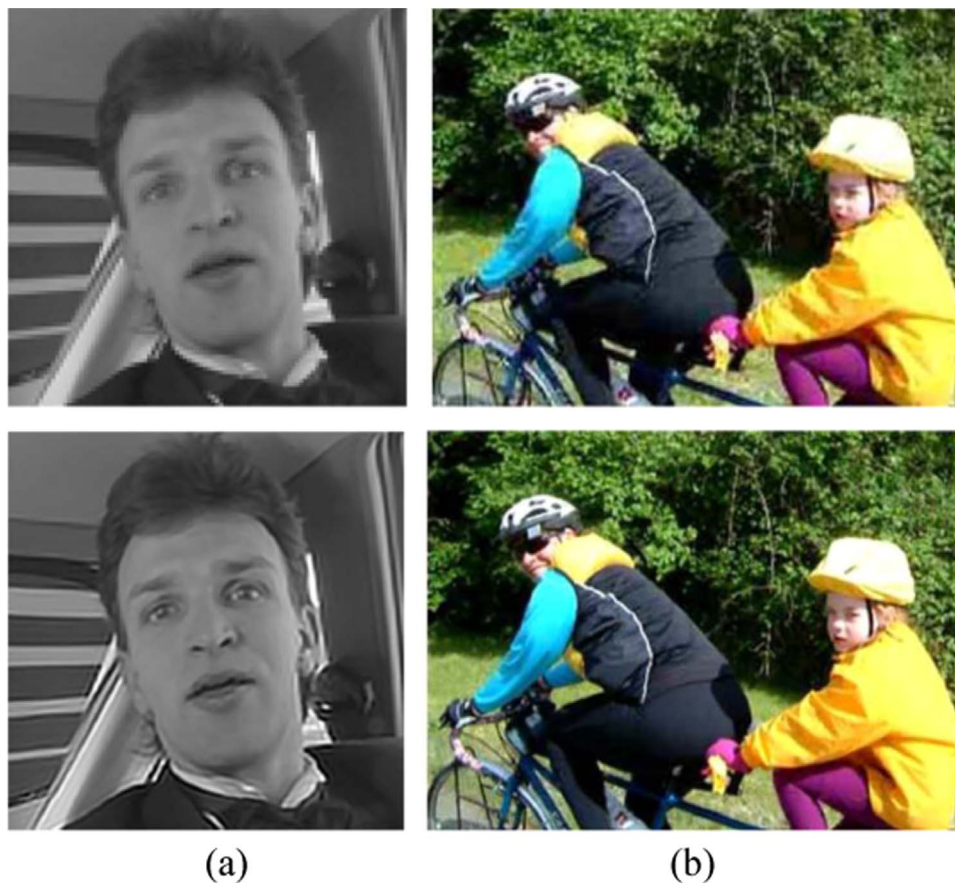
Fig. 10. The SR reconstruction of (a) a QCIF sequence [1] and (b) the *Bicycle* sequence [73]. The first row indicates the reference LR frames, while the second row presents the corresponding reconstruction results.
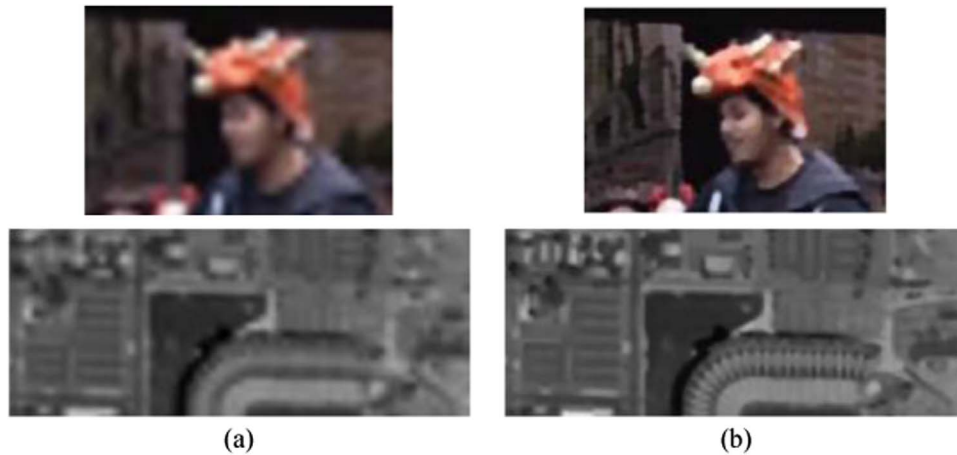
Fig. 11. The SR reconstruction of the *Walk* sequence (top row) [184] and a UAV surveillance sequence (bottom row) [66]: (a) indicates the reference LR frames, while (b) presents the corresponding reconstruction results.

We present the experimental results of single-image SR followed by down-sampling by a scale factor of 3. Fig. 9 shows the reconstructed HR *Girl* images by the use of different methods. With known degradation parameters, the TV reconstruction based method [47] is effective in recovering the texture, but it generates piecewise constant block artifacts. With external information learning, all the example-based SR methods can achieve effective reconstruction results in terms of visual plausibility, and obtain sharper edges. However, the NE method [156] has a limited ability to model visually complex texture, due to its high dependency on the quality of the samples in the database. The SC [11] approach expects to learn more effective information by constructing a joint dictionary. However, it is not sufficient to use a single mapping to describe the complex relationship between different image patch pairs. Exploiting nonlocal self-similarities between patches, learning mapping functions between patches, and employing reasonable assumptions for an image can allow better image recovery, as in the ASDS-AR-NL [159] and SPM [166] methods.

Furthermore, single-frame SR offers the potential to overcome the insufficient number of LR images, and has played a significant role in some specific domains such as face hallucination [173,174], license plate recognition [175], medical analysis [176,177], and satellite imaging [118], where diagnosis or analysis from few low-quality images can be extremely difficult.

3.3.3. Acceleration strategies for big data processing

There is a trend to use SR methods on large datasets, which are referred to as "big data". As a result, it is essential to develop methods that are both effective and efficient enough to satisfy the demand of the modern industrial applications.

Although abundant optimization methods have been proposed for fast SR (Section 3.2.6), the efficiency is still far away from the requirements of real-time applications. Other strategies for speed need to be developed. Zhang et al. [178] presented two methods for fast SR based on recursive multilevel reconstruction and parallel image reconstruction. It has to be mentioned that ADMM is well suited to parallelized mechanism for solving large-scale statistical tasks. Moreover, spatially adaptive block-based methods [73,179,180] are commonly used approaches. However, a deblocking process is always necessary to reduce the edge artifacts.

Alternatively, cloud computing is a simple and efficient solution, which can provide computing and storage services over the Internet [181]. Users can accomplish their goals on a very powerful computing platform employing a "super computer" [182].

4. Applications

After reviewing the methodologies above, let us return to the specific applications of SR in our daily life, which are the most basic concern. In the last three decades, various applications of SR have been addressed. In the following subsections, we give some examples of SR in the significant application fields.

4.1. Regular video information enhancement

The application of SR techniques has entered our daily life. LR video images can be converted to high-definition images using SR techniques. Hitachi Ltd. achieved the conversion of standard definition TV (SDTV) to high-definition television (HDTV) using SR technology for videos, which makes SR a particularly interesting and relevant research topic [183]. The related results can be found on the website http://www.engadget.com/2009/01/12/eyes-on-with-hitachi-super-resolution-tv/, where all the details in the frame are clearly enhanced.

Fig. 10 shows the SR results for some daily scenes. The QCIF video sequence was processed by 3-D ISKR [1], while the *Bicycle* sequence was handled by the method in [73]. These typical examples show the effectiveness of SR techniques when dealing with motion outliers caused by multiple moving objects, which is common in real scenes. Furthermore, Apple Inc. announced that they have applied for a patent of SR-based optical image stabilization. SR techniques will be employed in our phones, computers, and tablets someday sooner or later.

4.2. Surveillance

Nowadays, digital video recorder (DVR) devices are everywhere, and they play a significant role in applications such as traffic surveillance and security monitoring. It is, however, impossible for the moment to equip large-scale HR devices. Thus, it is necessary to study image SR techniques. Fig. 11 gives two examples of SR for the *Walk* sequence [184] and a UAV surveillance sequence [66]. Although the techniques have developed progressively, the practical use of video SR is still a challenge. Firstly, outdoor video devices are vulnerable to the impact of weather conditions. Moreover, video data usually feature a huge amount of data and complex motion. Some algorithms can deal with the motion outliers, but the computational efficiency limits their application. Compressed video SR has also been a focus [185,186].
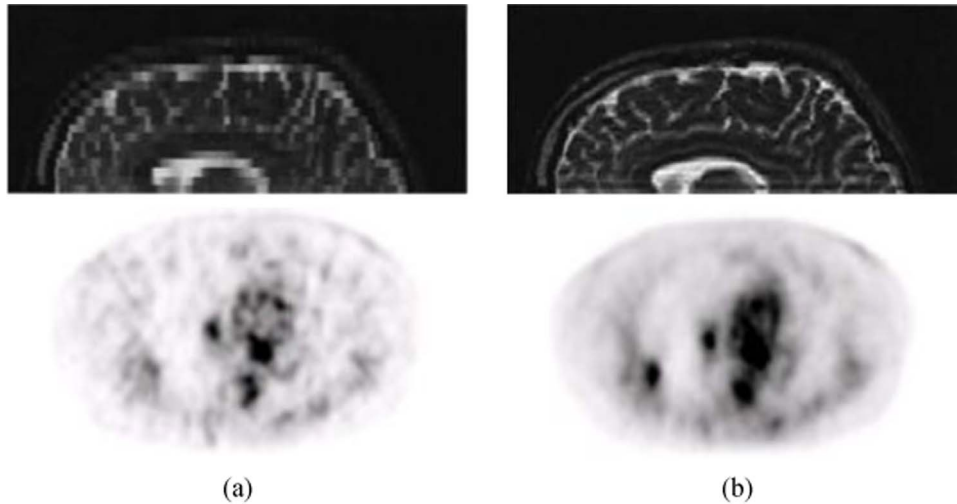
Fig. 12. The SR results of (a) an MRI [2] image and (b) a PET [67] image. The first column is the original LR images, and the second column shows the corresponding SR results.

4.3. Medical diagnosis

Various medical imaging modalities can provide both anatomical information about the human body structure and functional information. However, resolution limitations always degrade the value of medical images in the diagnosis. SR technologies have been used with the key medical imaging modalities, including magnetic resonance imaging (MRI), functional MRI (fMRI), and positron emission tomography (PET) [187]. The goal is to increase the resolution of medical images while preserving the true isotropic 3-D imaging. Medical imaging systems can be operated under highly controlled environments, and thus continuous and multi-view images can be easily acquired. Fig. 12 indicates the SR results on human brain MRI data [2] and a respiratory synchronized PET image, respectively [67].

Example-based SR for single frames has been also applied in the medical imaging field, by collecting similar images to establish a database [176,188]. The following example presented in Fig. 13 is the reconstructed image of the single MRI image of the knee in [176]. The training database was established with a set of five standard images, including computed tomography (CT) and MRI images from various parts of the human body.

4.4. Earth-observation remote sensing

As we know, the first SR idea in [31] was motivated by the requirement to improve the resolution of Landsat remote sensing images. The idea of applying SR techniques to remote sensing imaging has been developed for decades. Though data satisfying the demand for SR are not easy to obtain, there have been a few successful applicable examples for real data [25,27,28,189–191]. Among them, the resolution of the panchromatic image acquired by SPOT-5 can reach 2.5 m through the SR of two 5-m images obtained by shifting a double CCD array by half a sampling interval (Fig. 3), which was the most successful case [27,192]. In addition, Shen et al. [28] proposed a MAP algorithm and tested it with moderate-resolution imaging spectroradiometer (MODIS) remote sensing images, as shown in Fig. 14. Moreover, satellites can acquire multi-temporal or multi-view images for the same area, e.g. Landsat, CBERS, and WorldView-2, and thus provide the possibility for SR [25,191]. An example is also given in Fig. 14, which incorporates five angular images provided by the WorldView-2 satellite for SR [25]. SR for the spectral unmixing of fraction images has been widely studied to acquire a finer-resolution map of class labels, and is known as sub-pixel mapping [193–195]. Researchers have also attempted to apply the example-based methods to
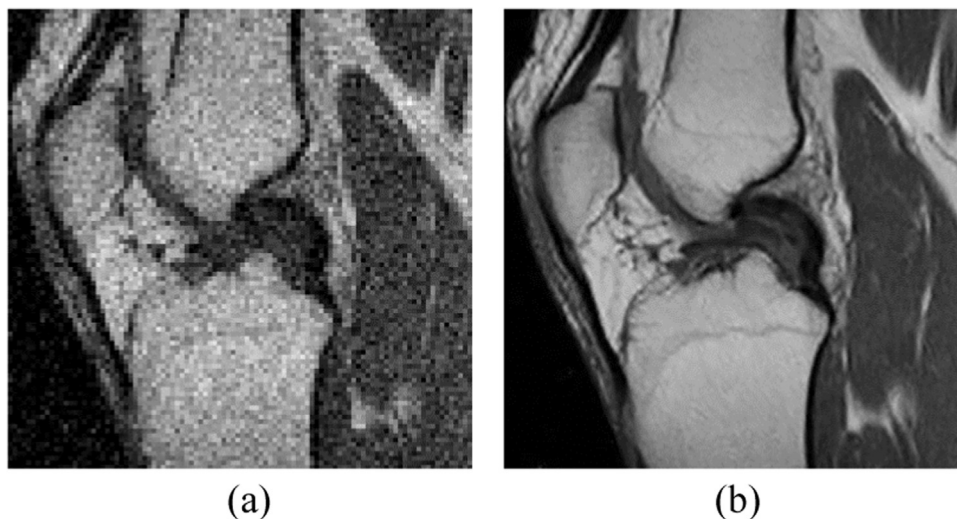
Fig. 13. The single-frame SR result on the MRI knee image with a magnification factor of 4 [176]. (a) The original LR data. (b) The SR result.

(a)   (b)
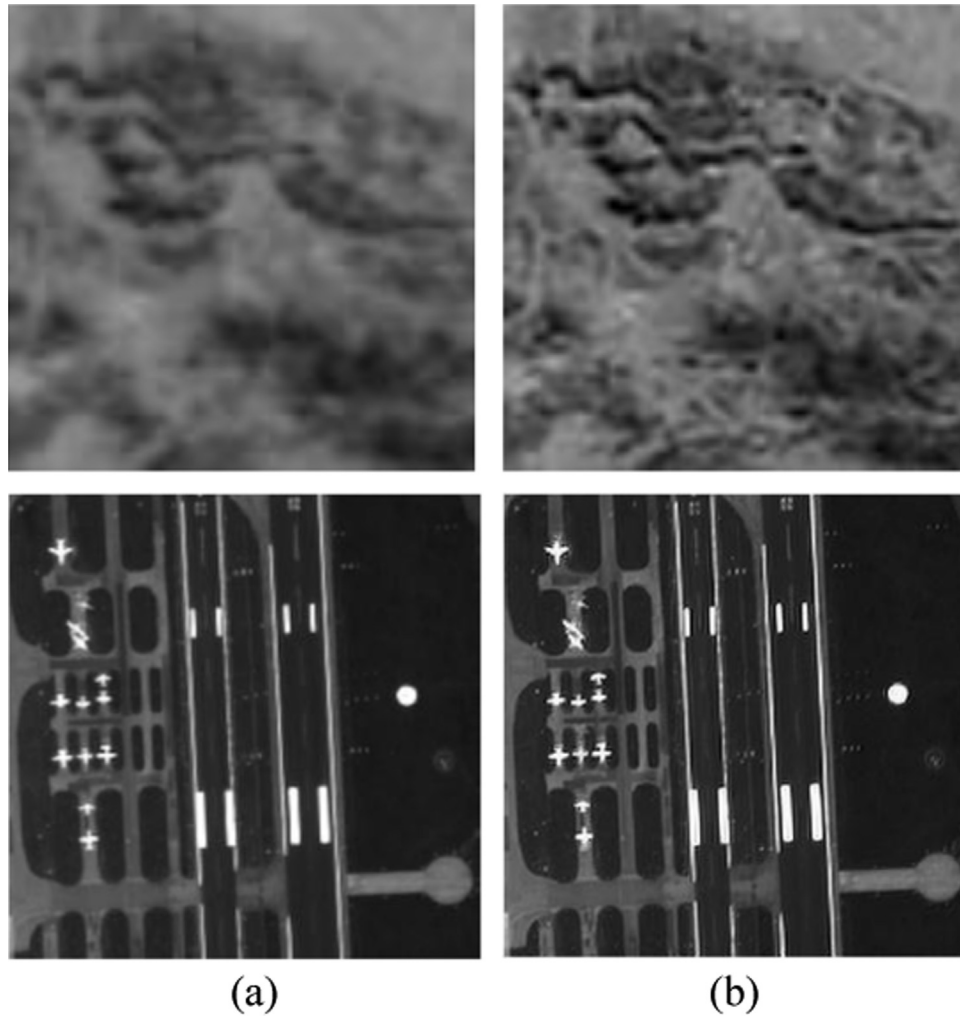
Fig. 14. The SR reconstruction of remote sensing images: (a) and (b) indicate the LR and HR images, respectively. The first row shows the test on multi-temporal MODIS images with a magnification factor of 2 [28]. The second row is the SR example for multi-angle WorldView-2 images with a magnification factor of 2 [25].

remotely-sensed image SR [196,197].

Recently, Skybox Imaging planned to launch a group of 24 small satellites, which can provide real-time "videos" with a sub-meter resolution using SR techniques [16,198]. At the moment, SkySat-1 and SkySat-2 have been launched and put into use. By incorporating approximately 20 frames, the ground-based distance (GSD) of the output image can be decreased to 4/5 of the original data [16]. This is a great opportunity to bring SR techniques into our daily life.

The main challenges for remotely-sensed image SR are to overcome the scene changes due to temporal differences, and to adapt the existing methods to massive amounts of observations every day.

4.5. Astronomical observation

The physical resolution of astronomical imaging devices limited by system parameters also provides a chance for SR techniques to play a role. Astronomical systems can typically collect a series of images for SR. By improving the resolution of astronomical images, SR can help astronomers with the exploration of outer space. A specific example is shown in Fig. 15 [64] showing the SR of

(a)   (b)
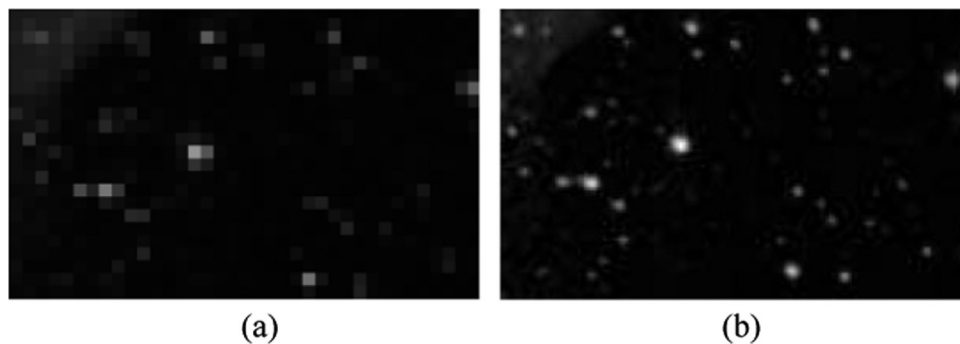
Fig. 15. SR example of astronomical images: (a) the original LR image and (b) the SR result.
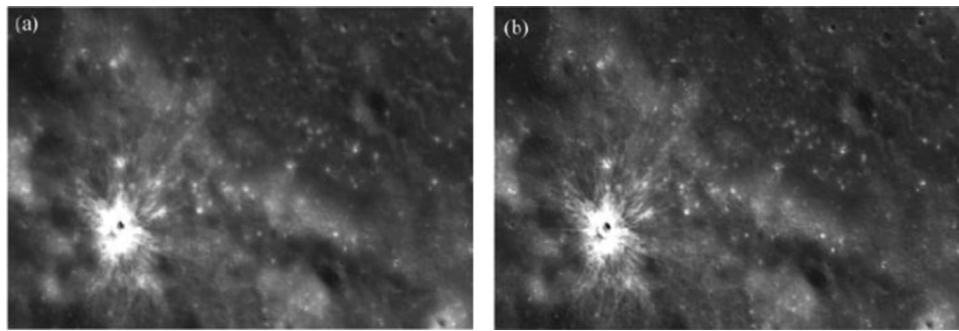
Fig. 16. The SR result of Chang'E-1 lunar images with a magnification factor of 2 [199]: (a) the original LR image and (b) the SR result.

multiple star images.

Satellites are also now being sent into outer space, e.g. the lunar exploration program and the Mars Odyssey mission. Fig. 16 indicates an SR example of Chinese Chang'E-1 lunar images [199], where the result was reconstructed based on three views. The SR can enhance the image resolution, and thus improve the discernibility of small objects on the moon's surface. Beyond this, Hughes and Ramsey [200] used Thermal Emission Imaging System (THEMIS) thermal infrared and visible datasets from different spectral regions to generate an enhanced thermal infrared image of the surface of Mars.

4.6. Biometric information identification

SR is also important in biometric recognition, including resolution enhancement for faces [24,201,202], fingerprints [203], and iris images [65,204]. The resolution of biometric images is pivotal in the recognition and detection process. To deal with the LR observations, a common approach is the development of high-quality images from multiple LR images. Based on the redundancy and similarity in the structured features of biometric images, example-based single-frame SR with an external database is an effective way of resolution enhancement [11]. We give three cases of biometric image reconstruction in Fig. 17 [203,205,206]. Using SR, the details of the shapes and structural texture are clearly enhanced, while the global structure is effectively preserved, which can improve the recognition ability in the relevant applications.

5. Discussion and conclusions

In this article, we intended to convey the concept, development, and main applications of super-resolution (SR) over the past three decades. The main progress in SR techniques can basically be divided into three stages. In the first decade, researchers shifted their attention from the study of frequency domain methods to spatial domain algorithms. Regularized multi-frame SR framework were the main focus in the second stage. The Bayesian MAP framework became the most popular technique due to its good performance and flexible characteristics. In recent years, however, the development of multi-frame SR has slowed down, and researchers have mainly focused on SR reconstruction in the various application fields. Unfortunately, the extensive practical use of SR
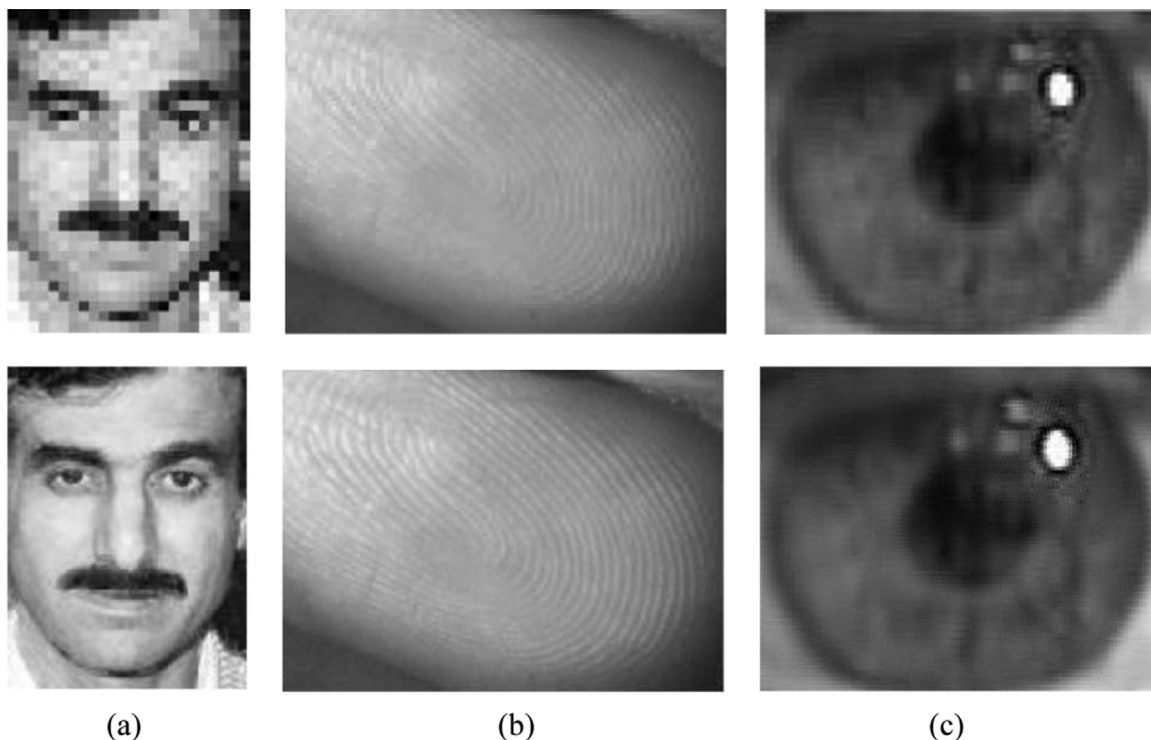
Fig. 17. The SR results for face [205], fingerprint [203], and iris images [189], respectively. The first row is the LR image, while the second row shows the reconstructed result. (a) Face hallucination, (b) fingerprint reconstruction, and (c) iris reconstruction.

still remains a problem. There has been a bottleneck-style dilemma in the development of multi-frame SR, while example-based SR for single images has become a hot issue. However, the performance of these algorithms depends on the reliability of the external database.

So what should we do in further studies? More advanced, adaptive, and faster methods with extensive applicability are always desirable. In addition, methods should be closely combined with actual requirements. The rapid development of hardware devices will also bring new challenges to the application of the SR framework. For instance, the Google Skybox project will provide us with an opportunity to obtain real-time HR "earth-observation videos" using remotely-sensed image SR. The concept of SR has also been extended to related fields such as fluorescence microscopy [17,207–209] and multi-baseline tomographic synthetic aperture radar (SAR) imaging [210,211]. Moreover, researchers have attempted to apply the single-frame SR techniques to the processing of medical and remote sensing imagery. However, the practicability of these methods is still limited by the relatively poor performance and time consumption, and acceleration strategies are essential for large-scale applications. In conclusion, the future of SR is still in our hands.

Acknowledgments

References

[1] H. Takeda, P. Milanfar, M. Protter, et al., Super-resolution without explicit subpixel motion estimation, IEEE Trans. Image Process. 18 (2009) 1958–1975.

[2] H. Greenspan, Super-resolution in medical imaging, Comput. J. 52 (2009) 43–63.

[3] J.A. Kennedy, O. Israel, A. Frenkel, et al., Super-resolution in PET imaging, IEEE Trans. Med. Imaging 25 (2006) 137–147.

[4] S.C. Park, M.K. Park, M.G. Kang, Super-resolution image reconstruction: a technical overview, IEEE Signal Process. Mag. 20 (2003) 21–36.

[5] S. Borman, R. Stevenson, Spatial Resolution Enhancement of Low-Resolution Image Sequences: A Comprehensive Review with Directions for Future Research, Laboratory for Image and Signal Analysis (LISA), University of Notre Dame, 1998 (Report, July).

[6] S. Farsiu, D. Robinson, M. Elad, et al., Advances and challenges in super-resolution, Int. J. Imaging Syst. Technol. 14 (2004) 47–57.

[7] M. Elad, A. Feuer, Super-resolution reconstruction of image sequences, IEEE Trans. Pattern Anal. Mach. Intell. 21 (1999) 817–834.

[8] K. Nasrollahi, T.B. Moeslund, Super-resolution: a comprehensive survey, Mach. Vis. Appl. 25 (2014) 1423–1468.

[9] D. Glasner, S. Bagon, M. Irani, Super-resolution from a single image, in 2009, in: Proceedings of the IEEE 12th International Conference on Computer Vision, 2009, pp. 349–356.

[10] K.I. Kim, Y. Kwon, Single-image super-resolution using sparse regression and natural image prior, IEEE Trans. Pattern Anal. Mach. Intell. 32 (2010) 1127–1133.

[11] J. Yang, J. Wright, T.S. Huang, et al., Image super-resolution via sparse representation, IEEE Trans. Image Process. 19 (2010) 2861–2873.

[12] W.T. Freeman, T.R. Jones, E.C. Pasztor, Example-based super-resolution, IEEE Comput. Graph. Appl. 22 (2002) 56–65.

[13] D. Capel, A. Zisserman, Computer vision applied to super resolution, IEEE Signal Process. Mag. 20 (2003) 75–86.

[14] J. Tian, K.K. Ma, A survey on super-resolution imaging, Signal, Image Video Process. 2011 (2011) 329–342.

[15] J. Van Ouwerkerk, Image super-resolution survey, Image Vis. Comput. 24 (2006) 1039–1052.

[16] K. Murthy, M. Shearn, B.D. Smiley, et al., SkySat-1: very high-resolution imagery from a small satellite, Sens., Syst., -Gener. Satell. XVIII (2014) (92411E-1–92411E-12).

[17] M.J. Rust, M. Bates, X. Zhuang, Sub-diffraction-limit imaging by stochastic optical reconstruction microscopy (STORM), Nat. Methods 3 (2006) 793–796.

[18] B. Shi, H. Zhao, M. Ben-Ezra, et al., Sub-pixel layout for super-resolution with images in the octic group, in: Proceedings of the European Conference on Computer Vision, ECCV, Springer 2014, pp. 250–264.

[19] M. Ben-Ezra, Z. Lin, B. Wilburn, et al., Penrose pixels for super-resolution, IEEE Trans. Pattern Anal. Mach. Intell. 33 (2011) 1370–1383.

[20] M. Pierre, Detection of visible photons in CCD and CMOS: a comparative view, Nucl. Instrum. Methods Phys. Res. Sect. A: Accel., Spectrom., Detect. Assoc. Equip. 504 (2003) 199–212.

[21] R.E. Coath, J.P. Crooks, A. Godbeer, et al., A low noise pixel architecture for scientific CMOS monolithic active pixel sensors, IEEE Trans. Nucl. Sci. 57 (2010) 2490–2496.

[22] M. Elad, Y. Hel-Or, A fast super-resolution reconstruction algorithm for pure translational motion and common space-invariant blur, IEEE Trans. Image Process. 10 (2001) 1187–1193.

[23] C. Latry, B. Rouge, Super resolution: quincunx sampling and fusion processing, in: Proceedings of the International Geoscience and Remote Sensing Symposium (IGARSS), Toulouse, France, 2003, pp. 315–317.

[24] Y. Zhuang, J. Zhang, F. Wu, Hallucinating faces: LPH super-resolution and neighbor reconstruction for residue compensation, Pattern Recognit. 40 (2007) 3178–3194.

[25] H. Zhang, Z. Yang, L. Zhang, et al., Super-resolution reconstruction for multi-angle remote sensing images considering resolution differences, Remote Sens. 6 (2014) 637–657.

[26] X. Zhang, E. Lam, E. Wu, et al., Application of Tikhonov regularization to super-resolution reconstruction of brain MRI images, Med. Imaging Inform. (2008) 51–56.

[27] H. Wang, D. Wen, The progress of sub-pixel imaging methods, in: Proceedings of the SPIE Conference Series, 2014, pp. 91420K-1.

[28] H. Shen, M.K. Ng, P. Li, et al., Super-resolution reconstruction algorithm to MODIS remote sensing images, Comput. J. 52 (2009) 90–100.

[29] B. Burke, P. Jorden, P. Vu, Overview paper-CCD technology, in: Scientific detectors for astronomy 2005, Springer, 2006, pp. 225–264.

[30] J.L. Harris, Diffraction and resolving power, J. Opt. Soc. Am. 54 (1964) 931–933.

[31] R.Y. Tsai, T.S. Huang, Multi-frame image restoration and registration, Adv. Comput. Vis. Image Process. 1 (1984) 317–339.

[32] D. Keren, S. Peleg, R. Brada, Image sequence enhancement using sub-pixel displacements, in: Proceedings of the Computer Society Conference on Computer Vision and Pattern Recognition, Ann Arbor, MI, USA, 1988, pp. 742–746.

[33] S.P. Kim, N.K. Bose, H.M. Valenzuela, Recursive reconstruction of high resolution image from noisy undersampled multiframes, IEEE Trans. Acoust., Speech, Signal Process. 38 (1990) 1013–1027.

[34] M.K. Ng, A.M. Yip, A fast MAP algorithm for high-resolution image reconstruction with multisensors, Multidimens. Syst. Signal Process. 12 (2001) 143–164.

[35] N. Nguyen, P. Milanfar, G. Golub, A computationally efficient superresolution image reconstruction algorithm, IEEE Trans. Image Process. 10 (2001) 573–583.

[36] Y. Altunbasak, A.J. Patti, R.M. Mersereau, Super-resolution still and video reconstruction from MPEG-coded video, IEEE Trans. Circuits Syst. Video Technol. 12 (2002) 217–226.

[37] S. Baker, T. Kanade, Limits on super-resolution and how to break them, IEEE Trans. Pattern Anal. Mach. Intell. 24 (2002) 1167–1183.

[38] S. Lertrattanapanich, N.K. Bose, High resolution image formation from low resolution frames using Delaunay triangulation, IEEE Trans. Image Process. 11 (2002) 1427–1441.

[39] S.C. Park, M.G. Kang, C.A. Segall, et al., Spatially adaptive high-resolution image reconstruction of low-resolution DCT-based compressed images, in: Proceedings of the IEEE International Conference on Image Processing, Rochester, New York, 2002, pp. 861–864.

[40] S. Farsiu, D. Robinson, M. Elad, et al., Robust shift and add approach to super-resolution, in: Proceedings of the SPIE – The International Society for Optical Engineering, San Diego, CA, United States, 2003, pp. 121–130.

[41] R. Molina, M. Vega, J. Abad, et al., Parameter estimation in Bayesian high-resolution image reconstruction with multisensors, IEEE Trans. Image Process. 12 (2003) 1655–1667.

[42] T. Akgun, Y. Altunbasak, R.M. Mersereau, Superresolution Reconstruction of Hyperspectral Images, Montreal, Que, Canada 2004, pp. 497–500.

[43] S. Farsiu, M.D. Robinson, M. Elad, et al., Fast and robust multiframe super resolution, IEEE Trans. Image Process. 13 (2004) 1327–1344.

[44] M.V. Joshi, S. Chaudhuri, R. Panuganti, Super-resolution imaging: use of zoom as a cue, Image Vis. Comput. 22 (2004) 1185–1196.

[45] C.A. Segall, A.K. Katsaggelos, R. Molina, et al., Bayesian resolution enhancement of compressed video, IEEE Trans. Image Process. 13 (2004) 898–910.

[46] M.K. Ng, A.C. Yau, Super-resolution image restoration from blurred low-resolution images, J. Math. Imaging Vis. 23 (2005) 367–378.

[47] M.K. Ng, H. Shen, E.Y. Lam, et al., A total variation regularization based super-resolution reconstruction algorithm for digital video, EURASIP J. Adv. Signal Process. 2007 (2007).

[48] M. Vega, J. Mateos, R. Molina, et al., Super-resolution of multispectral images, Comput. J. 52 (2009) 153.

[49] Q. Yuan, L. Zhang, H. Shen, et al., Adaptive multiple-frame image super-resolution based on U-curve, IEEE Trans. Image Process. 19 (2010) 3157–3170.

[50] J. Chen, J. Nunez-Yanez, A. Achim, Video super-resolution using generalized

Gaussian Markov random fields, IEEE Signal Process. Lett. 19 (2012) 63–66.

[51] H. Zhang, L. Zhang, H. Shen, A Super-resolution reconstruction algorithm for hyperspectral images, Signal Process. 92 (2012) 2082–2096.

[52] L. Yue, H. Shen, Q. Yuan, et al., A locally adaptive $L1 - L2$ norm for multi-frame super-resolution of images with mixed noise and outliers, Signal Process. 105 (2014) 156–174.

[53] C. Liu, D. Sun, On Bayesian adaptive video super resolution, IEEE Trans. Pattern Anal. Mach. Intell. 36 (2014) 346–360.

[54] H. Takeda, S. Farsiu, P. Milanfar, Kernel regression for image processing and reconstruction, IEEE Trans. Image Process. 16 (2007) 349–366.

[55] A. Tatem, H. Lewis, P. Atkinson, et al., Super-resolution land cover pattern prediction using a Hopfield neural network, Remote Sens. Environ. 79 (2002) 1–14.

[56] M. Irani, S. Peleg, Improving resolution by image registration, CVGIP: Graph. Model. Image Process. 53 (1991) 231–239.

[57] A.M. Tekalp, M.K. Ozkan, M.I. Sezan, High-resolution image reconstruction from lower-resolution image sequences and space-varying image restoration, in: Proceedings of the IEEE International Conference on Acoustics, Speech, and Signal Processing, 1992, pp. 169–172.

[58] R.R. Schultz, R.L. Stevenson, A Bayesian approach to image expansion for improved definition, IEEE Trans. Image Process. 3 (1994) 233–242.

[59] K. Aizawa, T. Komatsu, T. Saito, Acquisition of very high resolution images using stereo cameras, in: Proceedings of the Visual Communications, Boston, MA, 1991, pp. 318–328.

[60] S. Rhee, M.G. Kang, Discrete cosine transform based regularized high-resolution image reconstruction algorithm, Opt. Eng. 38 (1999) 1348–1356.

[61] N. Nguyen, P. Milanfar, A wavelet-based interpolation-restoration method for superresolution (wavelet superresolution), Circuits, Syst. Signal Process. 19 (2000) 321–338.

[62] H. Shen, L. Zhang, B. Huang, et al., A MAP approach for joint motion estimation, segmentation, and super resolution, IEEE Trans. Image Process. 16 (2007) 479–490.

[63] A.J. Patti, M.I. Sezan, A.M. Tekalp, High-resolution image reconstruction from a low-resolution image sequence in the presence of time-varying motion blur, in: Proceedings of the IEEE International Conference on Image Processing, Austin, TX, USA, 1994, pp. 343–347.

[64] R.M. Willett, I. Jermyn, R.D. Nowak et al., Wavelet-based superresolution in astronomy, Astronomical Data Analysis Software & Systems XIII, vol. 314, 2004, pp. 107.

[65] Y.-H. Li, Robust Long Range Iris Recognition from Video Using Super Resolution, Citeseer, 2010.

[66] Y. Wang, R. Fevig, R.R. Schultz, Super-resolution mosaicking of UAV surveillance video, in: Proceedings of the 15th IEEE International Conference on Image Processing, 2008, pp. 345–348.

[67] D. Wallach, F. Lamare, G. Kontaxakis, et al., Super-resolution in respiratory synchronized positron emission tomography, IEEE Trans. Med. Imaging 31 (2012) 438–448.

[68] H. Zhang, L. Zhang, H. Shen, A blind super-resolution reconstruction method considering image registration errors, Int. J. Fuzzy Syst. 17 (2015) 353–364.

[69] L. Zhang, H. Zhang, H. Shen, et al., A super-resolution reconstruction algorithm for surveillance images, Signal Process. 90 (2010) 848–859.

[70] H. Stark, P. Oskoui, High-resolution image recovery from image plane arrays, using convex projections, J. Opt. Soc. Am. A: Opt. Image Sci. Vis. 6 (1989) 1715–1726.

[71] M. Elad, A. Feuer, Restoration of a single superresolution image from several blurred, noisy, and undersampled measured images, IEEE Trans. Image Process. 6 (1997) 1646–1658.

[72] S.D. Babacan, R. Molina, A.K. Katsaggelos, Variational Bayesian super resolution, IEEE Trans. Image Process. 20 (2011) 984–999.

[73] H. Su, L. Tang, Y. Wu, et al., Spatially adaptive block-based super-resolution, IEEE Trans. Image Process. 21 (2012) 1031–1045.

[74] Y. Zhou, Z. Ye, Y. Xiao, A restoration algorithm for images contaminated by mixed Gaussian plus random-valued impulse noise, J. Vis. Commun. Image Represent. 24 (2013) 283–294 http://dx.doi.org/10.1016/j.jvcir.2013.01.004.

[75] H. Shen, X. Li, Q. Cheng, et al., Missing information reconstruction of remote sensing data: a technical review, IEEE Geosci. Remote Sens. Mag. 3 (2015) 61–85.

[76] Y.M. Huang, M.K. Ng, Y.W. Wen, A new total variation method for multiplicative noise removal, SIAM J. Imaging Sci. 2 (2009) 22–40.

[77] R.Z. Shilling, T.Q. Robbie, T. Bailloeul, et al., A super-resolution framework for 3-D high-resolution and high-contrast imaging using 2-D multislice MRI, IEEE Trans. Med. Imaging 28 (2009) 633–644.

[78] C. Bouman, K. Sauer, A generalized Gaussian image model for edge-preserving MAP estimation, IEEE Trans. Image Process. 2 (1993) 296–310.

[79] E.S. Lee, M.G. Kang, Regularized adaptive high-resolution image reconstruction considering inaccurate subpixel registration, IEEE Trans. Image Process. 12 (2003) 826–837.

[80] A. Marquina, S.J. Osher, Image super-resolution by TV-regularization and Bregman iteration, J. Sci. Comput. 37 (2008) 367–382.

[81] H. Shen, L. Peng, L. Yue, et al., Adaptive norm selection for regularized image restoration and super-resolution, IEEE Trans. Cybern. (2015), http://dx.doi.org/10.1109/TCYB.2015.2446755.

[82] H. Song, D. Zhang, P. Wang, et al., An adaptive L1–L2 hybrid error model to super-resolution, in: Proceedings of the 17th IEEE International Conference on Image Processing (ICIP), 2010, pp. 2821–2824.

[83] S. Cho, J. Wang, S. Lee, Handling outliers in non-blind image deconvolution, in: Proceedings of the IEEE International Conference on Computer Vision (ICCV), 2011, pp. 495–502.

[84] F. Suo, F. Hu, G. Zhu, Robust super-resolution reconstruction based on adaptive regularization, in: Proceedings of the International Conference on Wireless Communications and Signal Processing (WCSP), 2011, pp. 1–4.

[85] Y. Xiao, T. Zeng, J. Yu, et al., Restoration of images corrupted by mixed Gaussian-impulse noise via L1–L0 minimization, Pattern Recognit. 44 (2011) 1708–1720.

[86] X. Zeng, L. Yang, A robust multiframe super-resolution algorithm based on half-quadratic estimation with modified BTV regularization, Digit. Signal Process. 23 (2013) 98–109.

[87] H. Zhang, W. He, L. Zhang, et al., Hyperspectral image restoration using low-rank matrix recovery, IEEE Trans. Geosci. Remote Sens. 52 (2014) 4729–4743.

[88] Z. Wang, A.C. Bovik, H.R. Sheikh, et al., Image quality assessment: from error visibility to structural similarity, IEEE Trans. Image Process. 13 (2004) 600–612.

[89] Q. Yuan, L. Zhang, H. Shen, Regional spatially adaptive total variation super-resolution with spatial information filtering and clustering, IEEE Trans. Image Process. 22 (2013) 2327–2342.

[90] L. Zhang, H. Shen, W. Gong, et al., Adjustable model-based fusion method for multispectral and panchromatic images, IEEE Trans. Syst., Man., Cybern., Part B: Cybern. 42 (2012) 1693–1704.

[91] J. Sun, Z. Xu, H.-Y. Shum, Image super-resolution using gradient profile prior, in: Proceedings of the IEEE Conference on Computer Vision and Pattern Recognition, 2008, pp. 1–8.

[92] M.J. Beal, Variational Algorithms for Approximate Bayesian Inference, University of London, 2003.

[93] S. Osher, M. Burger, D. Goldfarb, et al., An iterative regularization method for total variation-based image restoration, Multiscale Model. Simul. 4 (2005) 460.

[94] Q. Yuan, L. Zhang, H. Shen, Multiframe super-resolution employing a spatially weighted total variation model, IEEE Trans. Circuits Syst. Video Technol. 22 (2012) 379–392.

[95] D. Bertaccini, R. Chan, S. Morigi, et al., An adaptive norm algorithm for image restoration, Scale Space and Variational Methods in Computer Vision, (2012) 194–205.

[96] X. Li, Y. Hu, X. Gao, et al., A multi-frame image super-resolution method, Signal Process. 90 (2010) 405–414.

[97] G. Gilboa, S. Osher, Nonlocal operators with applications to image processing, Multiscale Model. Simul. 7 (2008) 1005–1028.

[98] Z.J. Xiang, P.J. Ramadge, Edge-preserving image regularization based on morphological wavelets and dyadic trees, IEEE Trans. Image Process. 21 (2012) 1548–1560.

[99] A.N. Tikhonov, V.I.A. Arsenin, F. John, Solutions of Ill-posed Problems, Willey, New York, 1977.

[100] R.C. Hardie, K.J. Barnard, J.G. Bognar, et al., High-resolution image reconstruction from a sequence of rotated and translated frames and its application to an infrared imaging system, Opt. Eng. 37 (1998) 247–260.

[101] R. Pan, S.J. Reeves, Efficient Huber-Markov edge-preserving image restoration, IEEE Trans. Image Process. 15 (2006) 3728–3735.

[102] T. Goldstein, S. Osher, The split Bregman method for L1-regularized problems, SIAM J. Imaging Sci. 2 (2009) 323–343.

[103] L. Rudin, S. Osher, E. Fatemi, Nonlinear total variation based noise removal algorithms, Physica D 60 (1992) 259–268.

[104] J.M. Bioucas-Dias, M.A.T. Figueiredo, J.P. Oliveira, Total variation-based image deconvolution: a majorization-minimization approach, in: Proceedings of the IEEE International Conference on Acoustics, Speech and Signal Processing, 2006, pp. 861–864.

[105] M. Zhu, T. Chan, An efficient primal–dual hybrid gradient algorithm for total variation image restoration, UCLA CAM Report 08-34, 2008.

[106] T. Chan, C. Wong, Total variation blind deconvolution, IEEE Trans. Image Process. 7 (1998) 370–375.

[107] Y. Dong, M. Hintermüller, M.M. Rincon-Camacho, Automated regularization parameter selection in multi-scale total variation models for image restoration, J. Math. Imaging Vis. 40 (2011) 82–104.

[108] Q. Chen, P. Montesinos, Q.S. Sun, et al., Adaptive total variation denoising based on difference curvature, Image Vis. Comput. 28 (2010) 298–306.

[109] D. Strong, T. Chan, Edge-preserving and scale-dependent properties of total variation regularization, Inverse Probl. 19 (2003) S165.

[110] H. Zou, T. Hastie, Regularization and variable selection via the elastic net, J. R. Stat. Soc.: Ser. B (Stat. Methodol.) 67 (2005) 301–320.

[111] G. Steidl, S. Didas, J. Neumann, Relations between higher order TV regularization and support vector regression, Scale Space and PDE Methods in Computer Vision, Springer, 2005, pp. 515–527.

[112] Z. Xu, E.Y. Lam, Maximum a posteriori blind image deconvolution with Huber–Markov random-field regularization, Opt. Lett. 34 (2009) 1453–1455.

[113] M. Protter, M. Elad, H. Takeda, et al., Generalizing the nonlocal-means to super-resolution reconstruction, IEEE Trans. Image Process. 18 (2009) 36–51.

[114] G. Gilboa, S. Osher, Nonlocal linear image regularization and supervised segmentation, Multiscale Model. Simul. 6 (2007) 595–630.

[115] X. Zhang, M. Burger, X. Bresson, et al., Bregmanized nonlocal regularization for deconvolution and sparse reconstruction, SIAM J. Imaging Sci. 3 (2010) 253–276.

[116] J. Lu, H. Zhang, Y. Sun, Video super resolution based on non-local regularization and reliable motion estimation, Signal Process.: Image Commun. 29 (2014) 514–529.

[117] T. Sasao, S. Hiura, K. Sato, Super-resolution with randomly shaped pixels and

sparse regularization, in: Proceedings of the IEEE International Conference on Computational Photography (ICCP), 2013, pp. 1–11.

[118] Y. Zhao, J. Yang, Q. Zhang, et al., Hyperspectral imagery super-resolution by sparse representation and spectral regularization, EURASIP J. Adv. Signal Process. 2011 (2011) 1–10.

[119] Q. Yuan, L. Zhang, H. Shen, Hyperspectral image denoising employing a spectral-spatial adaptive total variation model, IEEE Trans. Geosci. Remote Sens. (2012).

[120] C.L. Lawson, R.J. Hanson, Solving Least Squares Problems, vol. 161, SIAM, 1974.

[121] P.C. Hansen, D.P. O'Leary, The use of the L-curve in the regularization of discrete ill-posed problems, SIAM J. Sci. Comput. 14 (1993) 1487–1503.

[122] G.H. Golub, M. Heath, G. Wahba, Generalized cross-validation as a method for choosing a good ridge parameter, Technometrics 21 (1979) 215–223.

[123] D. Krawczyk-StańDo, M. Rudnicki, Regularization parameter selection in discrete ill-posed problems – the use of the U-curve, Int. J. Appl. Math. Comput. Sci. 17 (2007) 157–164.

[124] N.K. Bose, S. Lertrattanapanich, J. Koo, Advances in superresolution using L-curve, in: Proceedings of the IEEE International Symposium on Circuits and Systems, 2001, pp. 433–436.

[125] H. He, L.P. Kondi, A regularization framework for joint blur estimation and super-resolution of video sequences, in: Proceedings of the IEEE International Conference on Image Processing, 2005, pp. 329–332.

[126] Y. He, K.-H. Yap, L. Chen, et al., A nonlinear least square technique for simultaneous image registration and super-resolution, IEEE Trans. Image Process. 16 (2007) 2830–2841.

[127] M. Seeger, D.P. Wipf, Variational Bayesian inference techniques, IEEE Signal Process. Mag. 27 (2010) 81–91.

[128] C. Vogel, M. Oman, Iterative methods for total variation denoising, SIAM J. Sci. Comput. 17 (1996) 227–238.

[129] P. Rodríguez, B. Wohlberg, Efficient minimization method for a generalized total variation functional, IEEE Trans. Image Process. 18 (2009) 322–332.

[130] P. Combettes, J.-C. Pesquet, Proximal splitting methods in signal processing, in: H.H. Bauschke, R.S. Burachik, P.L. Combettes, et al., (Eds.), Fixed-Point Algorithms for Inverse Problems in Science and Engineering, Springer, New York, 2011, pp. 185–212.

[131] S. Boyd, N. Parikh, E. Chu, et al., Distributed optimization and statistical learning via the alternating direction method of multipliers, Found. Trends Mach. Learn. 3 (2011) 1–122.

[132] R. Wolke, H. Schwetlick, Iteratively reweighted least squares: algorithms, convergence analysis, and numerical comparisons, SIAM J. Sci. Stat. Comput. 9 (1988) 907–921.

[133] J. Zhao, F. Shao, Y. Xu, et al., An improved Chan–Vese model without re-initialization for medical image segmentation, in: Proceedings of the 2010 3rd International Congress on Image and Signal Processing (CISP), 2010, pp. 1317–1321.

[134] B. Wahlberg, S. Boyd, M. Annergren, et al., An ADMM algorithm for a class of total variation regularized estimation problems, arXiv preprint arXiv:1203.1828, 2012.

[135] P.L. Combettes, J.-C. Pesquet, A Douglas–Rachford splitting approach o non-smooth convex variational signal recovery, IEEE J. Sel. Top. Signal Process. 1 (2007) 564–574.

[136] E. Esser, X. Zhang, T.F. Chan, A general framework for a class of first order primal–dual algorithms for convex optimization in imaging science, SIAM J. Imaging Sci. 3 (2010) 1015–1046.

[137] L.-L. Huang, L. Xiao, Z.-H. Wei, Efficient and effective total variation image super-resolution: a preconditioned operator splitting approach, Math. Probl. Eng. 2011 (2011) 20, http://dx.doi.org/10.1155/2011/380807.

[138] U. Mudenagudi, S. Banerjee, P.K. Kalra, Space-time super-resolution using graph-cut optimization, IEEE Trans. Pattern Anal. Mach. Intell. 33 (2011) 995–1008.

[139] T. Tung, S. Nobuhara, T. Matsuyama, Simultaneous super-resolution and 3D video using graph-cuts, in: Proceedings of the IEEE Conference on Computer Vision and Pattern Recognition, 2008, pp. 1–8.

[140] T. Brox, A. Bruhn, N. Papenberg, et al., High accuracy optical flow estimation based on a theory for warping, in: Proceedings of the Computer Vision-ECCV, Springer, 2004, pp. 25–36.

[141] G. Le Besnerais, F. Champagnat, Dense optical flow by iterative local window registration, in: Proceedings of the IEEE International Conference on Image Processing, 2005, pp. 137–140.

[142] G. D. Hager, P.N. Belhumeur, Real-time tracking of image regions with changes in geometry and illumination, in: Proceedings of the IEEE Computer Society Conference on Computer Vision and Pattern Recognition, CVPR, 1996, pp. 403–410.

[143] L. Baboulaz, P.L. Dragotti, Exact feature extraction using finite rate of innovation principles with an application to image super-resolution, IEEE Trans. Image Process. 18 (2009) 281–298.

[144] H. Su, Y. Wu, J. Zhou, Super-resolution without dense flow, IEEE Trans. Image Process. 21 (2012) 1782–1795.

[145] H. Hu, L.P. Kondi, An image super-resolution algorithm for different error levels per frame, IEEE Trans. Image Process. 15 (2006) 592–603.

[146] B.C. Tom, A.K. Katsaggelos, Reconstruction of a high-resolution image by simultaneous registration, restoration, and interpolation of low-resolution images, in: Proceedings of the IEEE International Conference on Image Processing, Washington, DC, USA, 1995, pp. 539–542.

[147] Y. Tian, K.-H. Yap, Joint image registration and super-resolution from low-resolution images with zooming motion, IEEE Trans. Circuits Syst. Video Technol. 23 (2013) 1224–1234.

[148] M. Protter, M. Elad, Super resolution with probabilistic motion estimation, IEEE Trans. Image Process. 18 (2009) 1899–1904.

[149] M. Irani, S. Peleg, Motion analysis for image enhancement: resolution, occlusion, and transparency, J. Vis. Commun. Image Represent. 4 (1993) 324–335.

[150] B.S. Morse, D. Schwartzwald, Image magnification using level-set reconstruction, in: Proceedings of the 2001 IEEE Computer Society Conference on Computer Vision and Pattern Recognition, 2001, pp. I-333–I-340.

[151] M.F. Tappen, B.C. Russell, W.T. Freeman, Exploiting the sparse derivative prior for super-resolution and image demosaicing, in: Proceedings of the IEEE Workshop on Statistical and Computational Theories of Vision, 2003.

[152] D. Shengyang, H. Mei, X. Wei, et al., Soft edge smoothness prior for alpha channel super resolution, in: Proceedings of the IEEE Conference on Computer Vision and Pattern Recognition, 2007, pp. 1–8.

[153] M. Ben-Ezra, Z. Lin, B. Wilburn, Penrose pixels super-resolution in the detector layout domain, in: Proceedings of the IEEE 11th International Conference on Computer Vision, 2007, pp. 1–8.

[154] Y.-W. Tai, S. Liu, M. S. Brown, et al., Super resolution using edge prior and single image detail synthesis, in: Proceedings of the IEEE Conference on Computer Vision and Pattern Recognition, 2010, pp. 2400–2407.

[155] H. Chang, D.-Y. Yeung, Y. Xiong, Super-resolution through neighbor embedding, in: Proceedings of the 2004 IEEE Computer Society Conference on Computer Vision and Pattern Recognition, 2004, pp. I–I.

[156] X. Gao, K. Zhang, D. Tao, et al., Image super-resolution with sparse neighbor embedding, IEEE Trans. Image Process. 21 (2012) 3194–3205, http://dx.doi.org/10.1109/tip.2012.2190080.

[157] X. Gao, K. Zhang, D. Tao, et al., Joint learning for single-image super-resolution via a coupled constraint, IEEE Trans. Image Process. 21 (2012) 469–480.

[158] K.I. Kim, Y. Kwon, Example-based learning for single-image super-resolution, Pattern Recognition, Springer, 2008, pp. 456–465.

[159] W. Dong, D. Zhang, G. Shi, et al., Image deblurring and super-resolution by adaptive sparse domain selection and adaptive regularization, IEEE Trans. Image Process. 20 (2011) 1838–1857.

[160] W.T. Freeman, E.C. Pasztor, O.T. Carmichael, Learning low-level vision, Int. J. Comput. Vis. 40 (2000) 25–47.

[161] M. Song, D. Tao, C. Chen, et al., Color to gray: visual cue preservation, IEEE Trans. Pattern Anal. Mach. Intell. 32 (2010) 1537–1552.

[162] T.-M. Chan, J. Zhang, J. Pu, et al., Neighbor embedding based super-resolution algorithm through edge detection and feature selection, Pattern Recognit. Lett. 30 (2009) 494–502.

[163] K. Zhang, X. Gao, X. Li, et al., Partially supervised neighbor embedding for example-based image super-resolution, IEEE J. Sel. Top. Signal Process. 5 (2011) 230–239.

[164] S. Yang, M. Wang, Y. Chen, et al., Single-image super-resolution reconstruction via learned geometric dictionaries and clustered sparse coding, IEEE Trans. Image Process. 21 (2012) 4016–4028.

[165] J. Yang, Z. Wang, Z. Lin, et al., Coupled dictionary training for image super-resolution, IEEE Trans. Image Process. 21 (2012) 3467–3478.

[166] T. Peleg, M. Elad, A statistical prediction model based on sparse representations for single image super-resolution, IEEE Trans. Image Process. 23 (2014) 2569–2582.

[167] K. Zhang, X. Gao, D. Tao, et al., Multi-scale dictionary for single image super-resolution, in: Proceedings of the IEEE Conference on Computer Vision and Pattern Recognition (CVPR), 2012, pp. 1114–1121.

[168] H. Zhang, Y. Zhang, T.S. Huang, Efficient sparse representation based image super resolution via dual dictionary learning, in: Proceedings of the IEEE International Conference on Multimedia and Expo (ICME), 2011, pp. 1–6.

[169] L. Xiaoqiang, Y. Haoliang, Y. Pingkun, et al., Geometry constrained sparse coding for single image super-resolution, in: Proceedings of the IEEE Conference on Computer Vision and Pattern Recognition (CVPR), 2012, pp. 1648–1655.

[170] S. Wang, D. Zhang, Y. Liang, et al., Semi-coupled dictionary learning with applications to image super-resolution and photo-sketch synthesis, in: Proceedings of the IEEE Conference on Computer Vision and Pattern Recognition (CVPR), 2012, pp. 2216–2223.

[171] R. Timofte, V. De, L.V. Gool, Anchored neighborhood regression for fast example-based super-resolution, in: Proceedings of the IEEE International Conference on Computer Vision (ICCV), 2013, pp. 1920–1927.

[172] C. Dong, C.C. Loy, K. He, et al., Learning a deep convolutional network for image super-resolution, in: Proceedings of the Computer Vision-ECCV, Springer, 2014, pp. 184–199.

[173] S. Baker, T. Kanade, Hallucinating faces, in: Proceedings of the IEEE International Conference on Automatic Face and Gesture Recognition, Grenoble, France, 2000, pp. 83–88.

[174] J. Yang, H. Tang, Y. Ma, et al., Face hallucination via sparse coding, in: Proceedings of the 15th IEEE International Conference on Image Processing, 2008, pp. 1264–1267.

[175] Y. Tian, K.-H. Yap, Y. He, Vehicle license plate super-resolution using soft learning prior, Multimed. Tools Appl. 60 (2012) 519–535.

[176] D.-H. Trinh, M. Luong, F. Dibos, et al., Novel example-based method for super-resolution and denoising of medical images, IEEE Trans. Image Process. 23 (2014) 1882–1895.

[177] L. Fang, S. Li, R.P. McNabb, et al., Fast acquisition and reconstruction of optical coherence tomography images via sparse representation, IEEE Trans. Med. Imaging 32 (2013) 2034–2049.

[178] D. Zhang, H. Li, M. Du, Fast, MAP-based multiframe super-resolution image reconstruction, Image Vis. Comput. 23 (2005) 671–679.

[179] R.S. Prendergast, T.Q. Nguyen, A block-based super-resolution for video sequences, in: Proceedings of the 15th IEEE International Conference on Image Processing, 2008, pp. 1240–1243.

[180] K. Simonyan, S. Grishin, D. Vatolin, et al., Fast video super-resolution via classification, in: Proceedings of the 15th IEEE International Conference on Image Processing, 2008, pp. 349–352.

[181] Y.S. Hu, X. Nan, P. Sengupta, et al., Accelerating 3B single-molecule super-resolution microscopy with cloud computing, Nat. Methods 10 (2013) 96–97.

[182] Z. Wenwu, L. Chong, W. Jianfeng, et al., Multimedia cloud computing, IEEE Signal Process. Mag. 28 (2011) 59–69, http://dx.doi.org/10.1109/msp.2011.940269.

[183] L. Hitachi, Super-resolution technology to convert video of various resolutions to high-definition. Available: ⟨http://www.hitachi.com/New/cnews/080924a.html⟩ (accessed 2008).

[184] C. Liu, D. Sun, A Bayesian approach to adaptive video super resolution, in: Proceedings of the IEEE Conference on Computer Vision and Pattern Recognition (CVPR), 2011, pp. 209–216.

[185] X. Zhang, M. Tang, R. Tong, Robust super resolution of compressed video, Vis. Comput. 28 (2012) 1167–1180.

[186] C.A. Segall, R. Molina, A.K. Katsaggelos, High-resolution images from low-resolution compressed video, IEEE Signal Process. Mag. 20 (2003) 37–48.

[187] M.D. Robinson, S.J. Chiu, J. Lo, et al., New Applications of Super-resolution in Medical Imaging, CRC Press, 2010.

[188] Y.-H. Wang, J. Qiao, J.-B. Li, et al., Sparse representation-based MRI super-resolution reconstruction, Measurement 47 (2014) 946–953.

[189] M.T. Merino, J. Nunez, Super-resolution of remotely sensed images with variable-pixel linear reconstruction, IEEE Trans. Geosci. Remote Sens. 45 (2007) 1446–1457.

[190] M. Elbakary, M. Alam, Superresolution construction of multispectral imagery based on local enhancement, IEEE Geosci. Remote Sens. Lett. 5 (2008) 276–279.

[191] J.C.-W. Chan, J. Ma, F. Canters, A comparison of superresolution reconstruction methods for multi-angle CHRIS/Proba images, SPIE Remote Sens. (2008) 710904-1–710904-11.

[192] K.H. Lim, L.K. Kwoh, Super-resolution for SPOT5-Beyond supermode, presented at the 30th Asian Conference on Remote Sensing, Beijing, China, 2009.

[193] Y. Zhong, L. Zhang, Remote sensing image subpixel mapping based on adaptive differential evolution, IEEE Trans. Syst., Man, Cybern., Part B: Cybern. 42 (2012) 1306–1329.

[194] D. Vikhamar, R. Solberg, Subpixel mapping of snow cover in forests by optical remote sensing, Remote Sens. Environ. 84 (2003) 69–82.

[195] Y. Ge, S. Li, V.C. Lakhan, Development and testing of a subpixel mapping algorithm, IEEE Trans. Geosci. Remote Sens. 47 (2009) 2155–2164.

[196] R.C. Patel, M. Joshi, Super-resolution of hyperspectral images using compressive sensing based approach, ISPRS Ann. Photogramm. Remote. Sens.

[197] Spat. Inf. Sci. 7 (2012) 83–88.

[197] F.A. Mianji, Y. Zhang, Y. Gu Resolution enhancement of hyperspectral images using a learning-based super-resolution mapping technique, in: Proceedings of the IEEE International Geoscience and Remote Sensing Symposium, 2009, pp. III-813–III-816.

[198] P. D'Angelo, G. Kuschk, P. Reinartz, Evaluation of skybox video and still image products, ISPRS Int. Arch. Photogramm., Remote Sens. Spat. Inf. Sci. XL-1 (2014) 95–99.

[199] L. Li, Q. Yu, Y. Yuan, et al., Super-resolution reconstruction and higher-degree function deformation model based matching for Chang'E-1 lunar images, Sci. China Ser. E: Technol. Sci. 52 (2009) 3468–3476.

[200] C.G. Hughes, M.S. Ramsey, Super-resolution of THEMIS thermal infrared data: compositional relationships of surface units below the 100 m scale on Mars, Icarus 208 (2010) 704–720.

[201] X. Wang, X. Tang, Hallucinating face by eigentransformation, IEEE Trans. Syst., Man, Cybern., Part C: Appl. Rev. 35 (2005) 425–434.

[202] W. Liu, D. Lin, X. Tang, Hallucinating faces: tensorpatch super-resolution and coupled residue compensation, in: Proceedings of the IEEE Computer Society Conference on Computer Vision and Pattern Recognition, 2005, pp. 478–484.

[203] Z. Yuan, J. Wu, S.-i. Kamata, et al., Fingerprint image enhancement by super resolution with early stopping, in: Proceedings of the IEEE International Conference on Intelligent Computing and Intelligent Systems, 2009, pp. 527–531.

[204] G. Fahmy, Super-resolution construction of iris images from a visual low resolution face video, in: Proceedings of the IEEE 9th International Symposium on Signal Processing and Its Applications, ISSPA 2007, pp. 1–4.

[205] W. Liu, D. Lin, X. Tang, Hallucinating faces: tensorpatch super-resolution and coupled residue compensation, in: Proceedings of the IEEE Computer Society Conference on Computer Vision and Pattern Recognition, CVPR, 2005, pp. 478-484.

[206] R. Barnard, V. Pauca, T. Torgersen, et al., High-resolution iris image reconstruction from low-resolution imagery, SPIE Opt.+Photonics (2006) (63130D-1–63130D-13).

[207] B. Huang, M. Bates, X. Zhuang, Super resolution fluorescence microscopy, Annu. Rev. Biochem. 78 (2009) 993.

[208] M. Bates, B. Huang, G.T. Dempsey, et al., Multicolor super-resolution imaging with photo-switchable fluorescent probes, Science 317 (2007) 1749–1753.

[209] G. Shtengel, J.A. Galbraith, C.G. Galbraith, et al., Interferometric fluorescent super-resolution microscopy resolves 3D cellular ultrastructure, Proc. Natl. Acad. Sci. 106 (2009) 3125–3130.

[210] X.X. Zhu, R. Bamler, Demonstration of super-resolution for tomographic SAR imaging in urban environment, IEEE Trans. Geosci. Remote Sens. 50 (2012) 3150–3157.

[211] F. Lombardini, M. Pardini, Superresolution differential tomography: experiments on identification of multiple scatterers in spaceborne sar data, IEEE Trans. Geosci. Remote Sens. 50 (2012) 1117–1129.